Korean J. Chem. Eng., 35(4), 875-889 (2018)
DOI: 10.1007/s11814-017-0335-3

pISSN: 0256-1115
eISSN: 1975-7220

Effects of process and design parameters on heat management in fixed bed Fischer-Tropsch synthesis reactor

Branislav Todic*,†, Milos Mandic*, Nikola Nikacevic, and Dragomir B. Bukur*,***,†**

*Chemical Engineering Program, Texas A&M University at Qatar, P. O. Box 23874, Doha, Qatar
**Faculty of Technology and Metallurgy, University of Belgrade, Karnegijeva 4, Belgrade, Serbia
***Texas A&M University, 3122 TAMU, College Station, Texas 77843, United States
(*Received 8 October 2017 • accepted 1 December 2017*)

Abstract−A two-dimensional pseudo-homogeneous model of wall-cooled fixed bed Fischer-Tropsch synthesis (FTS) reactor with Co/Re/γ-Al_2O_3 catalyst was developed to study the effect of process and design parameters on heat generation and removal characteristics. The influence of liquid-phase formation on heat transport was accounted for by using two-phase correlations. The effect of intraparticle diffusion on heat generation was considered. Detailed numerical simulations were performed to analyze the effect of process and design parameters on the reactor performance in terms of heat management. Results show that thermal behavior of FTS fixed bed reactors is very sensitive and any large disturbances can lead to temperature runaway. Large tube diameters are shown to be particularly unfavorable, with d_t>5 cm resulting in axial and radial gradients greater than 20 K and 13 K, respectively. The importance of detailed reactor modeling when designing and optimizing FTS fixed bed reactors is highlighted.

Keywords: Fischer-Tropsch Synthesis, Fixed Bed Reactor, Cobalt Catalyst, Heat Management

INTRODUCTION

Fischer-Tropsch synthesis (FTS) is a versatile technology and a key component of several processes for conversion of natural resources into liquid fuels and other high value products. These include conversion of natural gas, biomass and coal, which are first transformed into synthetic gas (or syngas, a mixture of carbon-monoxide and hydrogen) and then fed into an FTS reactor, where syngas is catalytically converted into a wide range of hydrocarbon molecules (mainly n-paraffin and 1-olefin).

The two general types of FTS technology are high and low temperature Fischer-Tropsch, (HTFT and LTFT) [1]. Temperatures typically used in HTFT are 320 to 350 °C, whereas LTFT usually operates in the 200 to 240 °C range. HTFT is a two-phase (gas-solid) process, where liquid exists only in catalyst particle pores, whereas LTFT is characterized by a three-phase (gas-liquid-solid) operation. HTFT is performed in fluidized-bed reactors, which are operated so that the liquid formation is minimized (high temperatures and lower values of chain growth parameter α). LTFT is mainly conducted in two types of commercial reactors: slurry bubble column (SBCR) and multi-tubular fixed bed reactors (MTFBR), both operating under three-phase (gas-liquid-solid) conditions. The selection of the type of FTS technology and reactors is based on several factors, including the desired products, and the natural resource used and its abundance at a given location.

MTFBRs are most often used as commercial FTS reactors. They are used in plants around the world, including South Africa, Qatar and Malaysia, as a part of Sasol ARGE and Shell Middle Distillate Synthesis process [1-3]. These reactors consist of several hundred to well over ten thousand tubes, with 2 to 5 cm in diameter. Due to the highly exothermic nature of FTS, relatively poor heat removal is considered as one of the main downsides to using the fixed bed reactor (FBR). Therefore, good heat transfer from the packed bed to the cooling fluid is a key factor in the optimal FTS FBR operation. Since iron is less active and therefore produces less heat, tubes up to 5 cm diameter are used with these catalysts, whereas for cobalt catalysts narrower tubes are more optimal. A part of the tail gas is often recycled into the reactor to limit per-pass conversion, thus limiting catalyst deactivation caused by high water partial pressure, while maintaining the overall conversion above 90%. This also helps to increase the gas velocity, thus improving the heat transfer coefficients. Several other ways to facilitate heat removal and/or decrease heat generation have also been proposed. Addition of inert gas (nitrogen) into the syngas feed was proposed to reduce the amount of generated heat by reducing partial pressures of reactants and to increase heat removal by increasing gas flowrates [4]. Unless accompanied by an appropriate total pressure increase, this would result in a loss of productivity. Commercial gasifiers produce syngas with a very low amount of inerts (<1%), so it is unlikely this approach is used in the industrial reactors. Recycling of produced liquid hydrocarbon has also been cited as a way to help boost heat removal [5,6]. Sie and Krishna [6] note that this is especially important in the region close to the inlet where temperature maximum is expected to occur and where the liquid is absent under typical operating conditions. However, the amount of liquid recycle needed to achieve this improvement in heat management and its utilization in the commercial plants was not discussed. Catalyst particles

†To whom correspondence should be addressed.
E-mail: branislav.todic@qatar.tamu.edu, dragomir.bukur@qatar.tamu.edu
Copyright by The Korean Institute of Chemical Engineers.

used in the FTS FBRs are in the 1 to 3 mm diameter range. Particles larger than about 0.2 mm are known to exhibit mass transfer limitations [7]. The use of large particles in MTFBRs is dictated by the need to maintain acceptable pressure drop within the tubes, even though this results in lower productivity per reactor volume.

A significant research effort has been focused on modeling of slurry-phase reactors for FTS, while modeling and design of fixed bed have received less attention [8,9]. The intricacies of conducting FTS in FBR are numerous and include trickle-bed behavior where the liquid produced during FTS trickles down the bed affecting heat and mass transfer, complex kinetics, large number of products etc. However, as noted by Steynberg et al. [8], there is no standard reaction engineering textbook which specifically covers FBR design for FTS. In the past, the number of modeling studies of conventional FTS fixed bed reactors was limited [4,10-12], but due to the surge of the topics' popularity it has significantly increased in recent years [13-25]. Modeling of fixed bed reactors for FTS over Fe-based catalyst was first done in the late 70's by Atwood and Bennett [10], by applying a simple kinetic model in a one-dimensional pseudo-homogeneous model of FBR. Later studies over iron utilized two-dimensional pseudo-homogeneous reactor models, assuming plug-flow and empirical kinetic and product selectivity models [4,11]. Wang et al. [12] applied detailed Langmuir-Hinshelwood-Hougen-Watson (LHHW) model of FTS kinetics, including reactant disappearance and product formation, as a part of one-dimensional heterogeneous FBR model. All of the above mentioned reactor modeling studies used Fe as catalyst of choice and neglected the effect of liquid formation on heat transfer. Several of the more recent studies considered models for Co-based catalysts [13-16,18,26,27], the majority of which used the 1-D modeling approach. A notable exception are several studies conducted by Jess and co-workers [19,20,24], who developed combined two-dimensional heat balance equations with one-dimensional mass balance and the catalyst particle model utilizing the catalyst effectiveness factor concept. Using textbook gas-phase fixed bed correlations for heat transfer parameters, they conducted an analysis of thermal behavior and suggested that 4 mm particle diameter and 4 cm tube diameter are the optimal choice for Co-based FTS in an FBR. Guettel and Turek [14] assumed liquid recycle and used trickle-bed correlation for heat transfer coefficient at the wall in a one-dimensional model of FBR [28]. Their results showed a reduced possibility of hot-spot formation compared to "dry" FBR. Studies with monolith reactors also showed a beneficial effect of recycling liquid products for a better temperature control [29,30]. The downside of using correlations developed for trickle-bed reactors in FTS reactor modeling is a potential for overestimation of the liquid phase effects. The correlation used by Guettel and Turek [14] predicts zero value of heat transfer coefficient at the reactor wall in the absence of liquid. However, considering that typically there is no liquid at FTS FBR inlet (i.e., no liquid recycle) and very little liquid throughout the bed, it is expected that such correlations would lead to severe underestimation of heat transfer coefficient at the wall by neglecting the influence of the gas phase contribution. Brunner et al. [15] suggested using trickle-bed correlations developed with consideration of low liquid flowrates for calculating an effective radial thermal conductivity [31]. In their one-dimensional FBR model the liquid formation rate was estimated from a simple Anderson-Schulz-Flory (ASF) product distribution. In fact, out of multiple studies which dealt with heat management, only Wang et al. [12] considered detailed FTS kinetics, albeit with the less active Fe catalyst. This enabled them to relate production of the full spectrum of FTS products with process conditions, as well as to determine the realistic amounts of gas and liquid phases and their composition. However, despite having detailed information on the liquid phase, Wang et al. [12] did not consider the effect of liquid phase generation on heat transport.

A two-dimensional model of conventional FTS FBR with Co-based catalyst has been developed in this study with the purpose of analyzing the heat management characteristics in such reactors. The model enables one to observe and analyze the interplay between a multitude of phenomena occurring in FTS FBRs under conditions similar to those used in the industrial practice. The main novelty of our model is that it includes detailed kinetics based on a highly active cobalt catalyst and a large number of product components, which are split between the gas and the liquid phase. The effect of the amount and the physical properties of the two phases on heat generation and removal characteristics are considered in detail. Even though the developed reactor model is capable of providing insight into the details of reactor performance, e.g., effect of process parameters on product selectivity and reactant conversion levels, this aspect of FTS FBRs has been extensively covered in the literature and is not the focus of the present study. Instead, model simulations were conducted to study the effect of process and design parameters (inlet temperature, pressure, feed ratio, syngas flowrate, cooling temperature, particle and tube diameters) on various aspects of FTS FBR heat management. Conservative assumptions about the feed composition were made : no liquid or gas recycle and no inert gases, thus minimizing the heat removal and maximizing the amount of generated heat.

MODELING METHODOLOGY

Guidelines for the design of FTS FBR based on industrial experience have been given by Steynberg et al. [8] These guidelines were carefully considered and utilized in the current work to create a reasonable representation of commercial FTS reactors. MTFBRs for FTS differ from the conventional gas-phase FBRs (e.g. those used in methanol synthesis) because a part of the products forms a liquid phase, which accumulates in the catalyst pellets and trickles down the reactor bed. As explained by Steynberg et al. [8], the volumetric production of liquid is low and its superficial velocity is typically below 1 mm/s, which ensures that the liquid flow is always in the trickle flow regime and well away from the pulse flow regime. However, FTS FBRs are also very different from conventional trickle-bed reactors (e.g. those used in hydrocracking or hydrodesulfurization), where volumetric liquid flowrates are significantly higher (liquid velocity >10 mm/s) [32]. Steynberg et al. [8] also note that the influence of liquid phase on FTS FBR hydrodynamics is relatively minor and that the pressure drop can be reasonably predicted using typical "dry" fixed bed correlations. However, the liquid has a major influence on the intra-particle diffusion coefficients, which can significantly reduce catalyst effectiveness compared to "dry" operation

[33]. As mentioned, the liquid phase also has an influence on heat transport processes in the reactor, where the presence of liquid is expected to have a positive effect.

Models of FTS FBR can be one- or two-dimensional, which is mainly dependent on expected radial temperature gradients. For smaller tube sizes (d_t<2.5 cm), Steynberg et al. [8] suggest that one-dimensional models are adequate for reactor design purposes. However, for larger diameter tubes, two-dimensional models are preferred due to considerably higher radial temperature gradients and their effect on the overall reactor performance in terms of conversion, selectivity and even temperature runaway. Since the goal of the current study is a detailed analysis of heat management, the two-dimensional approach was chosen, but comparisons with equivalent one-dimensional model results are also provided.

Conventional FTS FBR operates with a relatively slow volumetric reaction rates, so interfacial transport resistances can be neglected [8]. Therefore, pseudo-homogeneous models are acceptable as long as intra-particle transport resistances are taken into account. This can be done by considering the component effectiveness factor η_i, which is the ratio of volumetric average and surface value of consumption or formation rate for component i. Plug-flow assumption for FTS FBR models can be used considering typically used particle diameters (1-3 mm), tube diameters (1-5 cm), reactor lengths (6-12 m) and superficial gas-phase velocities (0.2-1 m/s) [8]. Axial dispersion is assumed to be negligible due to the use of a long reactor tube, small catalyst particles as well as relatively high gas velocities. Note that for process and design parameters used in this study, the axial Peclet number based on tube lengths is ~5000, which confirms that axial dispersion is negligible [34,35]. The ratio of tube and particle diameter (d_t/d_p) is typically above 10. Thus, radial voidage variation (wall effects) can also be neglected [36].

Inlet feed was considered to be comprised of pure syngas, without any inert or liquid/gas recycle. From a heat management perspective, this is a conservative assumption and will lead to a higher sensitivity of temperature gradients in relation to the process and design parameters.

1. Model Equations

The model is developed as a two-dimensional pseudo-homogeneous model without axial mixing, where intra-particle transport is taken into account via the component effectiveness factor η_i. Components considered in the system are CO, H_2, H_2O and hydrocarbons products CH_4, C_2, C_3, C_4, …, C_{24} and lumped C_{25+}. Hydrocarbon components are a summation of n-paraffin and 1-olefin products with the same carbon number. The model is described by a large number of equations, which could not all be presented here due to space limitations. In this section we provide the governing mass, heat and momentum balance equations, whereas the calculation of major parameters relating to heat management is described in Section 2. The remaining equations and parameters used are described in the Supplementary Material.

Two-dimensional mass balance is given by:

$$\frac{D_i^{er}}{u_s}\left(\frac{\partial^2(u_sC_i)}{\partial r^2}+\frac{1}{r}\frac{\partial(u_sC_i)}{\partial r}\right)-\frac{\partial(u_sC_i)}{\partial z}+\eta_i\rho_bR_i=0 \quad (1)$$

where C_i is the molar concentration of component i (i=CO, H_2, H_2O and hydrocarbons CH_4, C_2, …, C_{24} and lumped C_{25+}), z and r are axial and radial distances, D_i^{er} is the effective radial diffusivity of species i, u_s is superficial fluid velocity, η_i is the catalyst effectiveness for species i, ρ_b is reactor bed (bulk) density, and R_i is the rate of species i disappearance or formation. The effective radial diffusivity is calculated using Delmas and Froment correlation [37]. The equations for variables and values of parameters in Eq. (1) can be found in the Supplementary Material.

The parameters of kinetic models used in this study have been fitted to rate data obtained with a 0.48%Re-25%Co/Al_2O_3 catalyst, synthesized at the Center for Applied Energy Research (CAER) [38]. The rate of CO disappearance is calculated using the well-known kinetic model of Yates and Satterfield [39]:

$$(-R_{CO})=\frac{k\cdot P_{CO}\cdot P_{H_2}}{(1+a\cdot P_{CO})^2} \quad (2)$$

where $(-R_{CO})$ is the rate of CO disappearance; P_{CO}, P_{H_2}, P_{H_2O} are partial pressures of CO, H_2 and H_2O; k, a are kinetic parameters (parameter values provided in the Supplementary Material). The catalyst used in this study is about an order of magnitude more active than the catalyst used originally by Yates and Satterfield [39] and, therefore, more representative of catalysts used commercially. From the stoichiometry, the rate of H_2O formation is equal to the rate of CO consumption. The rate of H_2 disappearance is calculated based on the rate of CO disappearance and the usage ratio (UR) obtained from the product formation kinetics (for details see Supplementary Material). Methane and C_{2+} formation rates are calculated based on Ma et al. [40] and Todic et al. [41] kinetic models, respectively. All three kinetic models were fitted to the rate data obtained with the same 0.48%Re-25%Co/Al_2O_3 catalyst. All equations and parameters are provided in the Supplementary Material. The kinetic model of Todic et al. [41] provides a detailed kinetic representation of C_{2+} n-paraffin and 1-olefin formation and uses the concept of chain-length-dependent 1-olefin desorption to predict deviations of product distribution from the ASF distribution. The rates of C_{2+} n-paraffin and 1-olefin formation with the same number of C-atoms are summed up to give rates of lumped hydrocarbon components (C_2, C_3 etc.). Since this study considers a cobalt-based catalyst, the rate of water-gas shift reaction is assumed to be negligible. Reaction rates are normalized in order to maintain full atomic closures.

Heat balance equation is given by:

$$\lambda_{er}\left(\frac{\partial^2T}{\partial r^2}+\frac{1}{r}\frac{\partial T}{\partial r}\right)-u_s\rho C_p\frac{\partial T}{\partial z}+\eta_{CO}\rho_b(-\Delta H_r)(-R_{CO})=0 \quad (3)$$

where T is temperature, $(-\Delta H_r)$ is reaction enthalpy per mole of CO consumed, ρ is gas phase density, λ_{er} is effective radial thermal conductivity, η_{co} is the effectiveness factor for CO and C_p is gas phase heat capacity.

As mentioned, due to the presence of a small amount of liquid, its influence on hydrodynamics is minor and the use of "dry" bed correlations is considered appropriate for modeling of pressure drop in FTS FBRs [8]. Pressure drop is calculated using the Ergun correlation [42]:

$$-\frac{dP_t}{dz}=f\frac{\rho u_s^2}{d_p} \quad (4)$$

where P_t is total pressure, f is the friction factor for fluid flow in a packed bed and d_p is the particle diameter (calculation details are given in Supplementary Material). The same correlation was also used in a number of previous FTS FBR modeling studies [10,12, 19,21,23,26]. Furthermore, the use of gas phase pressure drop correlations is expected to result in somewhat lower pressure drops compared to the use of two-phase correlations. Thus, the total pressure and reactant partial pressures would be higher throughout the bed, leading to higher reaction rates and heat generation. Therefore, this can be considered as a conservative assumption from a heat management standpoint.

The boundary conditions needed to solve Eqs. (1), (3) and (4) are:

$$(z=0,\ 0\le r\le R_t) \qquad C_i=C_i^{in},\ u_s=u_s^{in} \tag{5}$$

$$(0<z\le L,\ r=0 \text{ and } r=R_t) \qquad \frac{\partial(u_s C_i)}{\partial r}=0 \tag{6}$$

$$(z=0,\ 0\le r\le R_t) \qquad T=T_{in} \tag{7}$$

$$(0<z\le L,\ r=0) \qquad \frac{\partial T}{\partial r}=0 \tag{8}$$

$$(0<z\le L,\ r=R_t) \qquad \lambda_{er}\frac{\partial T}{\partial r}=-h_{wall}(T-T_{wall}) \tag{9}$$

$$(z=0,\ 0\le r\le R_t) \qquad P=P_{in} \tag{10}$$

where L is reactor tube length, R_t is reactor tube radius, F_i^{in}, T_{in} and P_{in} are inlet flowrate of species i, inlet temperature and inlet pressure, respectively, h_{wall} is radial heat transfer coefficient at the wall and T_{wall} is wall temperature. It is assumed that the high flowrate of pressurized boiling water (cooling medium) in the outer shell ensures that wall temperature is equal along the reactor tube. Heat removed from the reactor tube is used to evaporate pressurized boiling water, producing steam and maintaining constant coolant temperature along the tube length [43]. Moreover, it is assumed that resistance to heat transfer from the wall to the cooling fluid can be neglected, as well as the heat transfer resistance through the steel tube wall, and thus wall temperature equals to that of the cooling fluid ($T_{wall}=T_{cool}$).

2. Parameters Determining Heat Generation and Removal

Parameters which are primarily responsible for determining the amount of heat generated in the fixed bed are FTS reaction enthalpy and reaction rates. The latter are affected by diffusional limitations, and this is taken into account through the effectiveness factor. The amount of heat being removed from the reactor depends on the effective radial heat conductivity and heat transfer at the wall. Therefore, procedures for calculation of these parameters are elaborated below.

2-1. FTS Reaction Enthalpy ($-\Delta H_r$)

Previous FTS studies used values of ($-\Delta H_r$) ranging from 147 to 180 kJ/mol CO to represent the FTS reaction enthalpy [4,13,16,44-46]. This parameter is important in determining the amount of heat generated in FTS reactor, and its value can vary depending on the assumed average product type and its molecular weight, i.e., on the product selectivity in general.

The value of FTS reaction enthalpy was analyzed considering different hydrocarbon products. The general stoichiometry of FTS can be expressed as:

$$CO+\left(1+\frac{m}{2n}\right)H_2\rightarrow\frac{1}{n}C_nH_m+H_2O \tag{11}$$

where m and n coefficients depend on the considered product. Reaction enthalpy at standard conditions is then calculated as:

$$\Delta H_r^{\theta}\left(\frac{kJ}{molCO}\right)=\frac{1}{n}H_f^{\theta}(C_nH_m)+H_f^{\theta}(H_2O)-H_f^{\theta}(CO)-\left(1+\frac{m}{2n}\right)H_f^{\theta}(H_2) \tag{12}$$

where H_f^{θ}(i) is standard enthalpy of formation of species i (i=CO, H_2, H_2O and C_nH_m). The reaction enthalpy at reaction condition (ΔH_r) can be calculated as [47]:

$$\Delta H_r=\Delta H_r^{\theta}+\Delta C_p(T-T^{\theta}) \tag{13}$$

where T^{θ} is standard temperature and ΔC_p is the overall change in heat capacity per mole of CO. Eq. (12) assumes that ΔC_p does not change with temperature. This parameter is determined by:

$$\Delta C_p=\frac{1}{n}C_p(C_nH_m)+C_p(H_2O)-C_p(CO)-\left(1+\frac{m}{2n}\right)C_p(H_2) \tag{14}$$

where C_p(i) is heat capacity of species i (i=CO, H_2, H_2O and C_nH_m). The values of standard enthalpies of formation, standard reaction enthalpies for various products, heat capacities at reaction temperature and overall change in heat capacity were obtained from literature [48] and are presented in Supplementary Material (Table S2). Fig. 1 shows the change of FTS reaction heat with carbon number at 473 K for different n-paraffin and 1-olefin species. We can see that the reaction heat for n-paraffin decreases from −212 kJ/mol CO for methane to −158 kJ/mol CO for $C_{20}H_{42}$. On the other hand, the reaction heat for 1-olefin increases from −112 kJ/mol CO for ethene to −148 kJ/mol CO for $C_{10}H_{20}$. Both n-paraffin and 1-olefin enthalpies converge to approximately −157 kJ/mol CO, which can be considered as FTS reaction heat per 1 mole of CH_2. This value is used in our calculations. The average FTS product under typi-

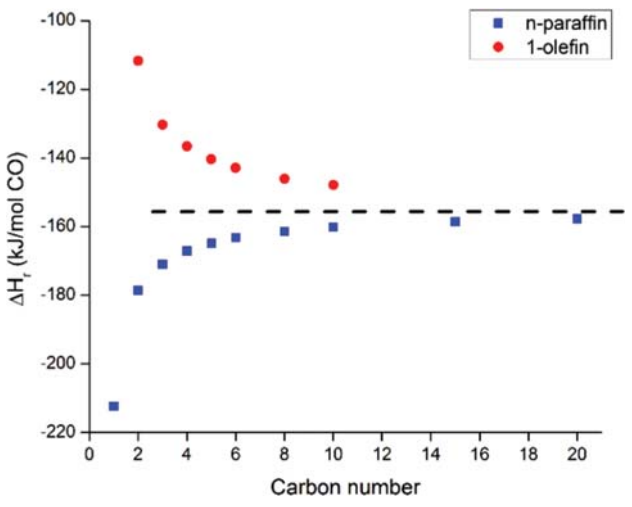

Fig. 1. FTS reaction enthalpy variation with carbon number.

cal reaction conditions is between C_6 and C_8, with about 20% 1-olefin and 80% n-paraffin selectivity, which also corresponds to the enthalpy value of approximately −157 kJ/mol.

Chaumette et al. [49] considered correction of the heat of reaction based on the enthalpy of condensation of C_{6+} hydrocarbons. They found that the overall enthalpy is increased by almost 2%. However, under realistic FTS conditions, the complete condensation of C_{6+} hydrocarbons is unlikely and the liquid phase consists mainly of higher molecular weight hydrocarbons (i.e., C_{20+}). Since these products are present in much smaller amounts, the contribution of condensation heat can be neglected.

2-2. Catalyst Effectiveness Factor (η)

Intra-particle mass transfer resistances can have a negative effect on FTS catalyst effectiveness and product selectivity. This topic was recently extensively covered for the catalyst used in this study by Mandic et al. [50]. Unlike its negative effect on the overall reactor productivity, a lower catalyst effectiveness factor has a positive effect on heat management, since less heat would be generated. Therefore, in this study we also considered the effect of catalyst effectiveness on heat management characteristics.

Based on the data provided by Mandic et al. [50], and additional calculations done by us, we found that there is a linear dependency between the effectiveness factor for CO consumption (η_{CO}) and the logarithm of generalized Thiele modulus (ϕ) in the diffusion controlled region (see Fig. 2). Note that, under typical ranges of FTS conditions, all fully loaded catalyst particles with diameters greater than approximately 1 mm will be in the diffusion controlled region. The effectiveness factor of CO for different process conditions and particle geometries was estimated from results for a single spherical catalyst particle as [50]:

$$\eta_{CO}=0.9939-0.469\cdot\ln(\phi) \tag{15}$$

where:

$$\phi=\frac{d_p}{6}\sqrt{\frac{\rho_p\cdot(-R_{CO})}{D_{e,CO}\cdot C^s_{CO}}} \tag{16}$$

where ρ_p is the catalyst particle density, $D_{e,CO}$ is the effective diffusivity of CO in wax, C^s_{CO} is the liquid phase concentration of CO at the catalyst particle surface, and $(-R^s_{CO})$ is the rate of CO disappearance at the catalyst surface. Diffusivity of CO in wax is calculated using a correlation developed by Akgerman and co-workers [51], while the CO liquid phase concentration is calculated from Henry's law and correlations provided by Marano and Holder [52]. Equations and parameter values are given in the Supplementary Material.

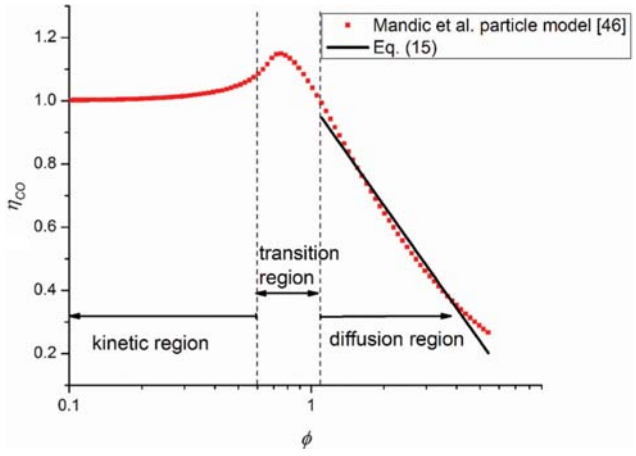

Fig. 2. CO effectiveness factor as a function of generalized Thiele modulus for spherical particle (T=473 K, P=2.5 MPa, H_2/CO ratio (FR)=2, X_{CO}=0).

It was assumed that the effectiveness factor for other components is equal to that of CO (i.e. $\eta_i=\eta_{CO}$) in mass balance Eq. (1). In the case of severe diffusion resistances, this assumption is correct only for H_2O, while H_2, CH_4 and some lighter hydrocarbons would have a slightly higher effectiveness factors than the CO, whereas higher hydrocarbons would have somewhat lower values of the effectiveness factor. This is due to shifts in FTS selectivity caused by changing the value of the intra-particle H_2/CO ratio. However, these selectivity variations and different η_i values could have only a minor influence on the thermal behavior of FTS FBRs. This would be reflected through minor changes in the heat of reaction due to a lower carbon-number of the average product and higher n-paraffin content, gas-phase physical properties (density, heat capacity and thermal conductivity) and velocity due to different composition, and the amount of liquid phase. Our group is currently working on relating selectivity variations to intra-particle resistances, but for the purposes of the current study of heat management in FBRs this can be neglected.

2-3. Radial Heat Transfer Coefficient at the Wall (h_{wall})

One of the main parameters that determine the rate of heat transfer in the FBR is a radial heat transfer coefficient at the wall. However, selection of an appropriate correlation for FTS in the FBR is not straightforward. Several studies suggest using the correlation of de Wash and Froment [8,15,34,53]:

$$h_{wall}=\frac{10.21\lambda_b}{d_t^{4/3}}+0.033\frac{\lambda_g}{d_p}Pr_gRe_g \tag{17}$$

where the first term represents the static and the second term the dynamic contribution to heat transfer at the wall. This correlation was developed for one-dimensional reactor models, where h_{wall} does not represent only resistance localized at the wall but the entire bed resistance in the radial direction [34], i.e. single parameter heat transfer model. Therefore, it is intrinsically not applicable for two-dimensional models, because it overestimates the resistance at the wall alone. Our calculations show that the correlation of de Wash and Froment [53] predicts values of h_{wall} that are significantly lower than the values obtained from correlations developed for two-dimensional models [54-59].

Another important issue is the need to account for the trickle-bed behavior: the effect of liquid on the value of h_{wall}. For example, Guettel and Turek [14] utilized Mariani et al. [28] trickle-bed correlation:

$$h_{wall}=\frac{\lambda_l}{d_p}\left[3.87-3.77\exp\left(-\frac{1.37d_p}{d_t}\right)\right]Pr_l^{1/3}Re_l^{0.643} \tag{18}$$

where the value of h_{wall} is entirely determined by liquid-phase flowrate and its properties. It is accepted in the literature that h_{wall} for conventional trickle-bed reactors is only dependent on the liquid-

phase and that the gas-phase influence can be neglected [60]. However, as explained above, conventional trickle-bed reactors operate with significantly higher liquid-phase flowrates than those expected in the FTS FBRs. Considering that there is almost no liquid in the zone close to the reactor inlet (a critical zone for hot-spot creation) and low amount of liquid throughout the reactor bed, it is not appropriate to use h_{wall} correlations developed for the conventional trickle-bed reactors.

The values of radial heat transfer coefficient at the wall (h_{wall}) for trickle-bed conditions under low liquid flowrates were reported by Matsuura et al. [61] Their results showed that the value of h_{wall} can be dependent on both gas and liquid phase flowrates. Two distinct regions were identified: a) region of low liquid flowrates (Re_l<10), where h_{wall} is predominantly determined by the gas phase flowrates; and b) region of high liquid flowrates (Re_l>10), where h_{wall} is predominantly determined by the liquid phase velocity and the gas phase velocity effect is negligible. Therefore, under typical FTS conditions (Re_l=0-2) h_{wall} can be assumed to be entirely determined by the gas phase velocities and typical gas-phase correlations apply. Note that with the recycle of liquid products, one could shift the values of h_{wall} towards the liquid velocity controlled region. However, as can be seen from the Re_l values, this would require a significant amount of liquid recycle (several times higher than produced in a single pass). Such high liquid flowrates at the inlet could have a very negative effect on the pressure drop. In the absence of information on the use of liquid recycle in commercial reactors for FTS, and as a conservative assumption in terms of heat management, the liquid recycle was not considered in our model.

A gas-phase correlation shown to adequately predict the two-parameter transport model h_{wall} value for a range of process conditions and fixed bed geometries was proposed by Specchia and Baldi [55] and is used in the present study:

$$h_{wall}=h_{wall,o}+h'_{wall,g} \tag{19}$$

where $h_{wall,o}$ and $h'_{wall,g}$ are stagnant and convective contributions, respectively. These can be calculated as:

$$h_{wall,o}=\frac{\lambda_g}{d_p}\left(2\varepsilon_b+\frac{1-\varepsilon_b}{\frac{\lambda_g}{\lambda_s}\gamma_w+\phi_w}\right) \tag{20}$$

$$h'_{wall,g}=\frac{\lambda_g}{d_p}\cdot 0.0835\cdot Re_g^{0.91} \tag{21}$$

Parameters γ_w=1/3 and ϕ_w=0.00240·$(d_t/d_p)^{1.58}$ are used for spherical particles [55]. The remaining parameters in Eqs. (20) and (21) are defined in the Supplementary Material.

2-4. Effective Radial Thermal Conductivity (λ_{er})

The second parameter determining the overall resistance to radial heat transport in two-dimensional models is the effective radial thermal conductivity in the reactor core (λ_{er}). Experimental values of this parameter under trickle-bed conditions at low liquid flowrates were reported by Matsuura et al. [31]. Similar to other trickle-bed studies, they considered the static contribution of heat transport by conduction and diffusion inside the packed bed (λ^s_{er}) and the dynamic contributions of convective heat transfer in the gas- and the liquid-phase (λ^s_{er}, λ^l_{er}):

$$\lambda_{er}=\lambda^s_{er}+\lambda^g_{er}+\lambda^l_{er} \tag{22}$$

Matsuura et al. [31] assumed that the λ^s_{er}/λ_l ratio is constant for moist fixed bed, i.e., independent from the liquid holdup and particle diameter, and from experiments determined the relation for stationary contribution as:

$$\lambda^s_{er}=1.5\lambda_l \tag{23}$$

where λ_l is thermal conductivity of the liquid layer in the reactor. The values of λ^g_{er} and λ^l_{er} are related to the radial mixing of gas and liquid phases inside the packed bed, and can be expressed as a function of Reynolds and Prandtl numbers:

$$\lambda^g_{er}+\lambda^l_{er}=(\alpha\beta)_g\lambda_g\,Re_g\,Pr_g+(\alpha\beta)_l\lambda_l\,Re_l\,Pr_l \tag{24}$$

where coefficients appearing in Eq. (24) are defined in the Supplementary Material.

3. Solution Methodology

The model equations were solved using the gPROMS ModelBuilder 4.2 software package. This software discretizes partial derivatives in spatial dimensions and simultaneously solves the model as a large system comprised of blocks of linear and non-linear algebraic equations.

The model equations and variables were discretized in axial and radial directions, using first-order backward finite difference method with 50 points and second-order orthogonal collocation on finite elements method with 10 points, respectively. Because axial temperature profiles tend to change rapidly close to the reactor inlet, a non-uniform logarithmic grid with larger density at the start of the axial domain was used. The transformation function is:

$$z'=\frac{\ln(\alpha z+1)}{\ln(\alpha+1)} \tag{25}$$

where coefficient α=7. After discretization, the model consisted of almost 150,000 algebraic equations, which were sorted into blocks and solved simultaneously by gPROMS proprietary algorithms.

To ensure model solution convergence, an initialization procedure was applied. It consisted of the sequential solution of simplified model equations with gradually increasing complexity until the full model is reached. Additional details are provided in the Supplementary Material.

RESULTS AND DISCUSSION

1. Base Case Parameters

Reactor model simulations were performed using different inlet process conditions, catalyst particle and reactor tube diameters. To compare the influence of variations of these parameters on the reactor heat management characteristics, a set of base parameters were used as a reference. The base case parameters are: T_{in}=473 K, T_{wall}=T_{in}, P_{in}=2.5 MPa, feed H_2/CO ratio (FR)=2, F_{in}=0.150 mol/s (u_s^{in}=0.45 m/s, GHSV=2.73 NL/(g_{cat}·h)), d_p=2 mm, d_t=2.6 cm and L=10 m. These conditions result in CO conversion (X_{CO}) and C_{5+} selectivity (S_{C5+}) of 28% and 87%, respectively. The corresponding pressure drop is 0.18 MPa. Unless specifically noted, only one parameter was varied in different simulations, while others were kept at their

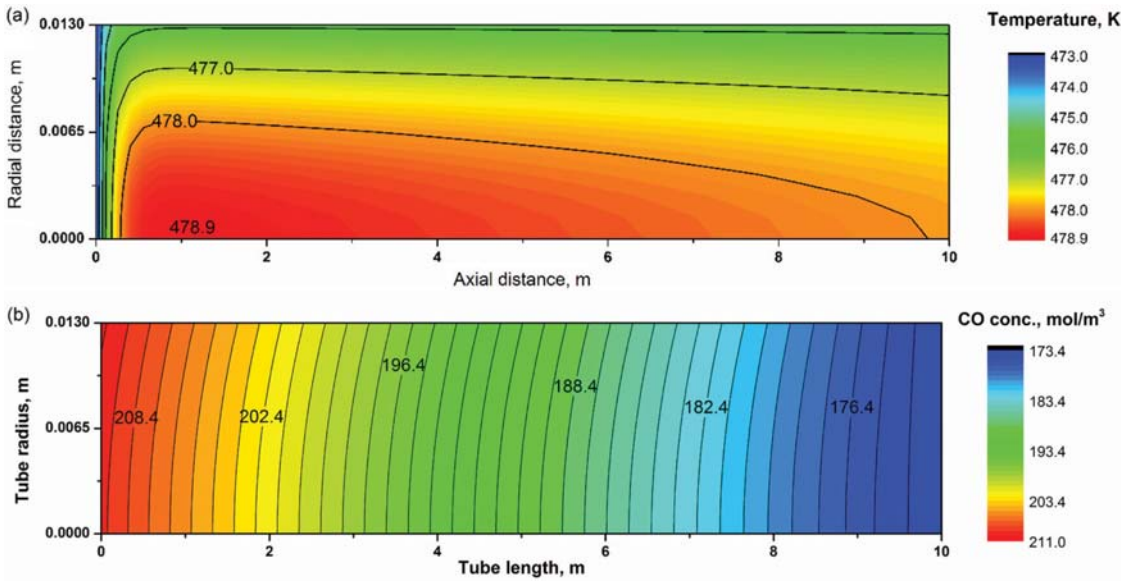

Fig. 3. Results of 2-D reactor model simulations for base case conditions (T_{in}=473 K, T_{wall}=T_{in}, d_p=2 mm, d_t=2.6 cm, P_{in}=2.5 MPa, feed H_2/CO ratio (FR)=2, F_{in}=0.15 mol/s, u_s^{in}=0.45 m/s and η_i=0.43-0.53): (a) Temperature distribution in axial and radial direction; (b) gas phase CO concentration distribution in axial and radial direction.

base case values.

Fig. 3 shows the temperature and concentration distribution predicted by the 2-D reactor model. From Fig. 3(a) the temperature maximum (hotspot) is located close to the reactor inlet (z<2 m) and the radial gradient of temperature at that position is about 3 K for the base case conditions. The occurrence of a temperature maximum at this location is consistent with the findings in previous literature studies [62,63]. Temperature rise in the axial direction in this case is nearly 6 K. This can be explained by a much higher reaction rate close to the reactor inlet due to high partial pressures of reactants. In the middle and bottom parts of the bed, the reactant partial pressures are lower and, therefore, reaction rates and heat generation can be significantly lower as well. The difference between the temperature at the wall (T(r=R_t)) and the wall (coolant) temperature rises quickly close to the reactor inlet, but soon reaches a value of about 3 K, which is then maintained throughout the length of the bed. The average radial heat transfer coefficient at the wall (h_{wall}) is 947 W/(m^2·K) and the average effective radial thermal conductivity (λ_{er}) is 6.6 W/(m·K), for the base case conditions, which is consistent with literature reports [6].

These are significant temperature differences, which can have implications on FTS reaction rate and selectivity. Fig. 3(b) shows that the change in CO concentration in the radial direction is very small, and that the significant concentration gradient exists only in the axial direction. This means that a simplification of mass balance to 1-D, as was done in some previous studies [4,18-20,24], is in fact justified in the case of a plug flow reactor.

2. Comparison of One- and Two-dimensional Models for FTS Fixed Bed Reactor

Computation time required to solve the 2-D reactor model is significantly higher compared to the 1-D model. Therefore, care has to be taken in analyzing the necessity of the 2-D approach. Also, considering that the majority of previously published studies utilized the 1-D approach, it is interesting to see how results from the 1-D model compare to those of the 2-D model.

An equivalent 1-D reactor model can be described by the following mass and energy balance equations [34]:

$$-\frac{d(u_s C_i)}{dz} = \eta \rho_b R_i \tag{26}$$

$$u_s \rho c_p \frac{dT}{dz} = (-\Delta H_r)\,\eta \rho_b (-R_{CO}) - \frac{4U}{d_t}(T - T_{wall}) \tag{27}$$

where all boundary conditions at z=0 and parameters are defined in the same way as for the 2-D model. The overall heat transport coefficient (U) is defined as [34]:

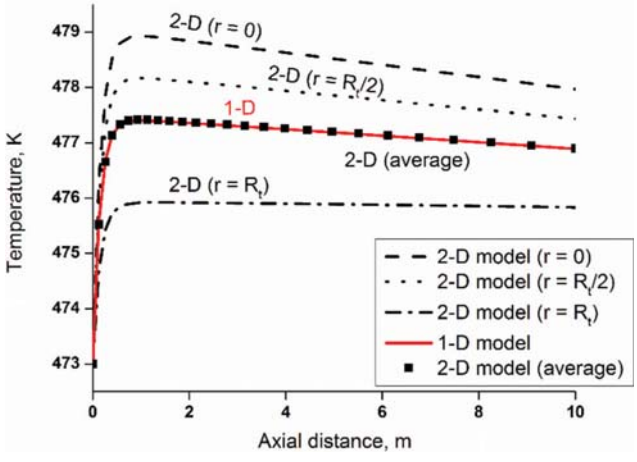

Fig. 4. Comparison of axial temperature distribution in 1-D and 2-D reactor model for base case conditions (T_{in}=473 K, T_{wall}=T_{in}, P_{in}=2.5 MPa, FR=2, F_{in}=0.150 mol/s, u_s^{in}=0.45 m/s, d_p=2 mm and d_t=2.6 cm).

$$\frac{1}{U}=\frac{1}{h_{wall}}+\frac{d_t}{8\lambda_{er}} \quad (28)$$

where h_{wall} and λ_{er} are calculated based on the same equations as in the 2-D model (Eqs. (19) and (22)).

Fig. 4 shows a comparison between 2-D and 1-D axial temperature profiles. The 2-D results for temperature distribution are shown at three distinct radial positions: reactor core (r=0), midpoint (r=R_t/2) and wall (r=R_t). We see that the assumption of uniform (1-D) temperature distribution provides considerably different results compared to individual radial positions (2-D model). To assess the effect of this assumption on the reactor performance we compared the two most important performance indicators, CO conversion and C_{5+} productivity, at the same process conditions. Even though the 2-D reactor model results show a very pronounced radial gradient compared to the 1-D reactor model, the differences in terms of conversions and productivity for the base case conditions are minor. The 2-D model predicts CO conversion of 27.74%, compared to 27.73% for the 1-D model, while the calculated C_{5+} productivities are $6.12\cdot10^{-4}$ mol/s (2-D model), and $6.13\cdot10^{-4}$ mol/s (1-D model). This high degree of similarity between the 2-D and 1-D results at these conditions can be explained considering the average cross-section temperature of the 2-D reactor bed ($T_{ave}(z)=\frac{1}{A_{cs}}\int_0^{R_t}2r\pi T(z,r)dr$), which almost coincides with the axial temperature profile for the 1-D reactor model (Fig. 4). We have made comparisons between the two models at other conditions as well and results are typically very similar. Larger differences in conversion level and productivity exist only when the system approaches temperature runaway conditions. For example, simulations for d_t=5.8 cm (other parameters correspond to base case) show that 1-D and 2-D model result in different conversions, with X_{CO}=32.84% and 34.05%, respectively. In this case the axial temperature profiles also differ for the 1-D and 2-D model, with about 2 K difference at the temperature peak. This behavior suggests that Eq. (28) overall provides a very good prediction of the overall heat transport coefficient, which is consistent with the fact that the calculated Biot number is low (Bi=$h_{wall}R_t/\lambda_{er}$~2 for the base case) [64]. Biot number quantifies the ratio between the radial bed resistance and the heat transfer resistance in the wall region. The low value of Bi implies that the majority of thermal resistance is located close to the reactor wall and that radial temperature gradients are less important. Differences in model predictions from the 1-D and 2-D models become more apparent only for conditions where higher temperature gradients occur (in the region of higher Biot numbers), which in our case is for reactor tube diameters above 5 cm.

Therefore, the importance of using a 2-D reactor model in the analysis of heat management (temperature profiles and hotspots, heat generation and removal, temperature runaway etc.) is highlighted. However, for detailed simulation studies focusing on the prediction of the overall FTS reactor performance the equivalent 1-D model can be used for a small reactor tube diameters.

The use of the equivalent one-dimensional approach enables one to define the overall resistance to heat transport in the radial direction (1/U) and compare it to contributions of bed resistance

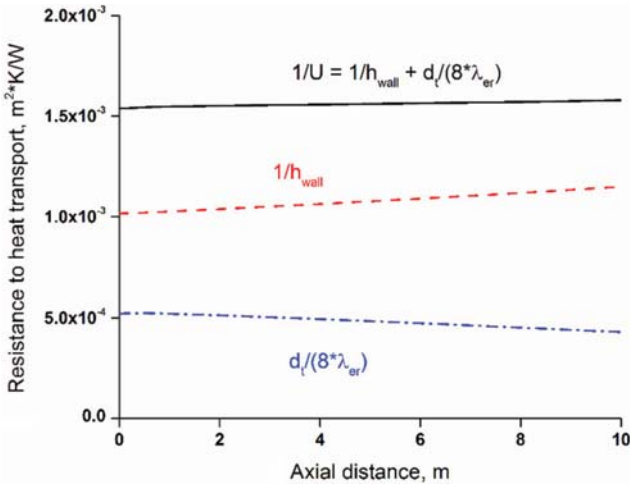

Fig. 5. Overall heat resistance and its wall and bed components along the reactor length (base case conditions) (T_{in}=473 K, T_{wall}=T_{in}, P_{in}=2.5 MPa, FR=2, F_{in}=0.150 mol/s, u_s^{in}=0.45 m/s, d_p=2 mm and d_t=2.6 cm).

in the radial direction ($dt/(8\cdot\lambda_{er})$) and the resistance located close to the wall ($1/h_{wall}$). For the base case conditions the contribution of resistance in the wall region is dominant, and is approximately two-times higher than that of the bed resistance (Fig. 5), which is consistent with often used assumption that the majority of resistance is located close to the tube wall [34]. The overall resistance remains relatively constant throughout the reactor and its values are similar to those reported by Brunner et al. [15] using similar values of process parameters. However, the two constituent resistances (the bed and the wall-region resistance) exhibit changes along the reactor length, which is related to changes of physical properties of the gas phase and generation of the liquid phase. This is discussed in more detail below.

3. Accounting for the Catalyst Effectiveness and its Influence on Heat Management

One of the major factors in determining the amount of heat generated during FTS is the catalyst effectiveness. For our base case with d_p=2 mm, representing typical FTS geometry and conditions, the catalyst effectiveness factor goes from 0.53 at the reactor inlet to 0.43 at the outlet. The unlikely scenario of having η_i=1 with d_p= 2 mm was compared to the base case results in terms of maximum axial (the middle of the reactor tube) temperature (Fig. 6). Results show that for η_i=1 at the base case conditions, the temperature increases rapidly near the reactor inlet and runaway occurs. Therefore, the existence of intra-particle diffusion resistance significantly reduces the amount of heat generated in the reactor, thereby decreasing the likelihood of temperature runaway. However, this is done at the expense of reducing reactor productivity per catalyst mass. Additional results illustrating the relationship between the particle size, catalyst effectiveness and heat management are presented in Section 3.5.

One way to maintain high catalyst utilization, while having reduced heat generation, is to use spherical particles with an eggshell distribution of the catalyst. Lower catalyst loading due to the use of eggshell distribution can be described by modifying the mass and heat balance equations (Eqs. (1) and (3)):

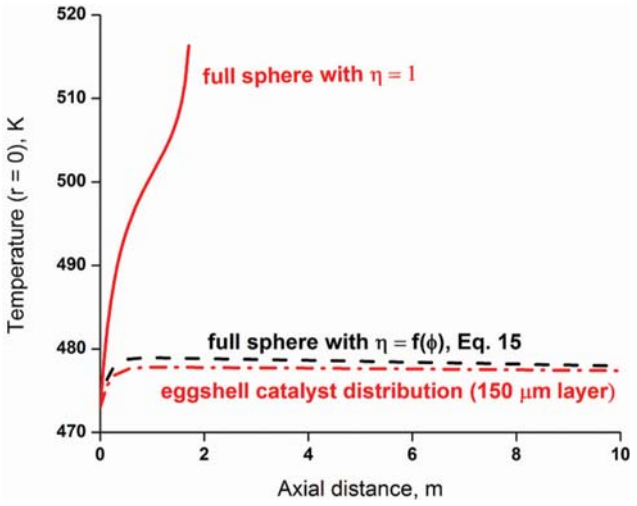

Fig. 6. Comparison of axial core temperature distribution for different effectiveness levels (η=1 and η varied based on its dependence from process conditions and particle size) and catalyst distribution (T_{in}=473 K, T_{wall}=T_{in}, P_{in}=2.5 MPa, FR=2, F_{in}=0.150 mol/s, u_s^{in}=0.45 m/s, d_p=2 mm and d_t=2.6 cm; for eggshell catalyst distribution layer thickness is δ=150 μm).

$$\frac{D_i^{er}}{u_s}\left(\frac{\partial^2(u_sC_i)}{\partial r^2}+\frac{1}{r}\frac{\partial(u_sC_i)}{\partial r}\right)-\frac{\partial(u_sC_i)}{\partial z}+\left(1-\frac{(r_p-\delta)^3}{r_p^3}\right)\rho_b R_i=0 \quad (29)$$

$$\lambda_{er}\left(\frac{\partial^2 T}{\partial r^2}+\frac{1}{r}\frac{\partial T}{\partial r}\right)-u_s\rho C_p\frac{\partial T}{\partial z}+\left(1-\frac{(r_p-\delta)^3}{r_p^3}\right)\rho_b(-\Delta H_r)(-R_{CO})=0 \quad (30)$$

where δ represents the thickness of the catalyst layer in a spherical particle and r_p is the particle radius. The term $\left(1-\frac{(r_p-\delta)^3}{r_p^3}\right)$ represents the volume fraction of the spherical particle occupied by the catalyst. For small values of layer thickness (δ<200 μm) and our catalyst, it can be assumed that the catalyst effectiveness is approximately 1.

The effect of using the catalyst with eggshell distribution and 150 μm thickness, under the base case conditions, on the temperature profile is shown in Fig. 6. We can see that using the eggshell catalyst distribution results in a similar (slightly lower) temperature gradient compared to the fully loaded catalyst particle. The CO conversion with the eggshell catalyst is also lower (23.2%). This similarity in performance can be explained by considering the amount of catalyst loaded into the reactor and the effectiveness of its utilization. Only 39 vol% of the particle is filled with the catalyst in the case of 2 mm particle with 150 μm thick eggshell distribution, but the catalyst effectiveness is 1. On the other hand with the completely filled catalyst particle the catalyst effectiveness is about 0.45 (an average value for the entire reactor). Therefore, using catalysts with eggshell distribution does not seem to have a significant influence on heat management characteristics, but enables achieving similar conversions with much less catalyst in the reactor.

4. Effect of Inlet Process Conditions and the Wall Temperature on Temperature Distribution

We analyzed the effect of three process conditions directly

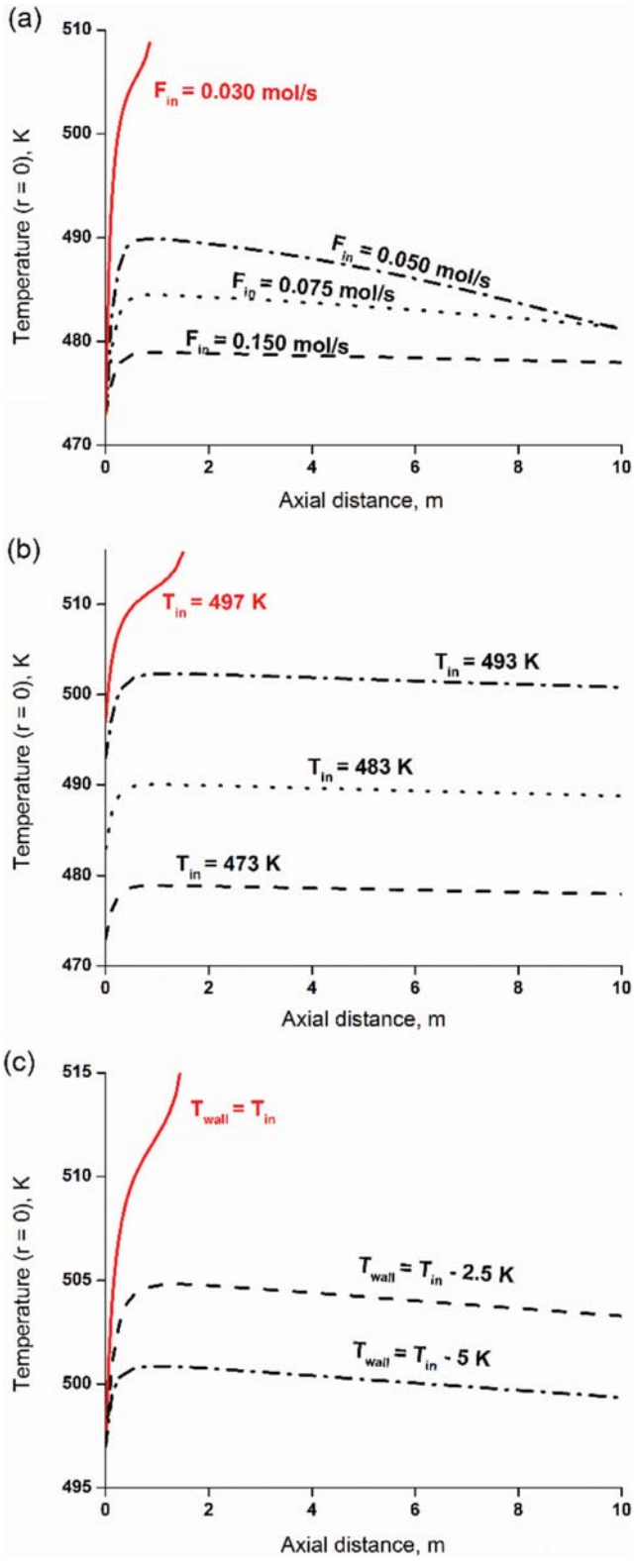

Fig. 7. Effect of varying inlet process conditions on core temperature distribution: (a) Inlet flowrate (T_{in}=473 K, T_{wall}=T_{in}, P_{in}=2.5 MPa, feed H_2/CO ratio (FR)=2, u_s^{in}=0.09-0.45 m/s, d_p=2 mm and d_t=2.6 cm); (b) inlet temperature (T_{wall}=T_{in}, P_{in}=2.5 MPa, FR=2, F_{in}=0.150 mol/s, u_s^{in}=0.45 m/s, d_p=2 mm and d_t=2.6 cm); (c) wall temperature at T_{in}=497 K (P_{in}=2.5 MPa, FR=2, F_{in}=0.150 mol/s, u_s^{in}=0.45 m/s, d_p=2 mm and d_t=2.6 cm).

related to the rates of heat generation and its removal: inlet molar flowrate (F_{in}), inlet temperature (T_{in}) and wall temperature (T_{wall}). Results of 2-D model simulations in which one of these parameters is varied while keeping the other process and design parameters constant are summarized in Fig. 7.

Fig. 7(a) shows the influence of varying the inlet flowrate (i.e. inlet velocity) on the reactor thermal behavior. If all other process parameters are kept constant at the base case conditions, decreasing the inlet flowrate from 0.150 mol/s to 0.050 mol/s (inlet velocity from 0.45 to 0.15 m/s) results in poorer heat removal and the maximum temperature increases from about 479 K to 490 K. Further reduction of inlet flowrate (e.g. to 0.030 mol/s, i.e. 0.09 m/s) results in an inability of the system to remove generated heat and temperature runaway occurs. Similar behavior was reported by Wang et al. [12] for FTS conducted in FBRs with Fe-based catalyst, who varied the inlet velocity by changing the recycle ratio. This behavior is related to the influence of gas and liquid phase velocities on the heat transfer coefficient at the wall (h_{wall}) and radial thermal conductivity (λ_{er}). Considering Eqs. (19)-(21), h_{wall} is only affected by the gas phase velocity (Re_g), and liquid phase generation does not influence this parameter. Increasing Re_g (inlet flowrate) will result in an increase of h_{wall} (Fig. 8(a)). Typical values of h_{wall} go from 200 to above 1,000 W/(m^2K) and are not only determined by the flowrate, but also by the physical properties of the gas phase mixture (density, viscosity and thermal conductivity). Since the composition of the gas phase changes along the reactor the change of mixture physical properties has to be taken into account when calculating heat transport parameters. A good way to illustrate this is by looking at the relationship of h_{wall} and the conversion level. Fig. 8(a) shows the value of h_{wall} along the reactor for several simulations in which F_{in} was varied. Because of relatively low pressure drop and low conversion levels in all simulations, gas phase Reynolds number does not change significantly. For the base case (F_{in}=0.150 mol/s, X_{CO}=27%) Re_g is 296 and 303 at the inlet and exit, respectively, which is a small change and does not influence the h_{wall} value in a major way. However, h_{wall} does decrease along the reactor (984 to 870 W/(m^2K) for the base case) due to changes of gas mixture thermal conductivity. These results suggest that operating at higher conversions could have a detrimental effect on h_{wall} values. Similarly, the change of λ_{er} along the reactor for different values of is F_{in} is shown in Fig. 8(b). λ_{er} is positively affected by increasing Re_g, but there the liquid phase formation and its velocity also plays a role. Liquid phase velocity inside the reactor can be expressed in terms of liquid phase Reynolds number (Re_l), which typically varies between 0 and 1. From Fig. 8(b) we see that the liquid phase formation has an exceptionally positive effect on λ_{er}, whose value can be increased by 50% or more along the reactor. For base case conditions λ_{er} goes from 6.22 W/(m·K) at the reactor inlet to 7.56 W/(m·K) at the outlet. This increase can be directly related to the increase of Re_l at higher conversion levels. Considering that at the base conditions the resistance of radial heat transport in the reactor core comprises about 1/3 of the overall heat transport resistance (Fig. 5), it is evident that accounting for the liquid formation and its influence on λ_{er} can improve the model accuracy.

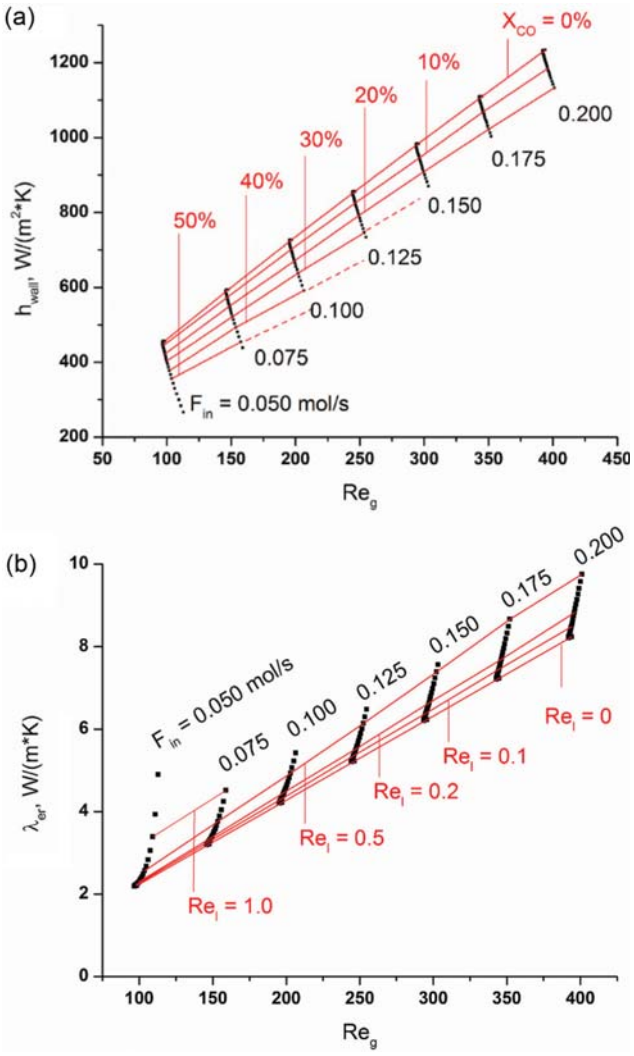

Fig. 8. (a) Dependency between heat transfer coefficient at the wall (h_{wall}) and gas phase Reynolds number at different conversion levels; (b) dependency between radial thermal conductivity (λ_{er}) and gas and liquid phase Reynolds numbers (T_{in}= 473 K, T_{wall}=T_{in}, P_{in}=2.5 MPa, FR=2, u_s^{in}=0.15-0.60 m/s, d_p=2 mm and d_t=2.6 cm).

Fig. 7(b). Increasing T_{in} results in an increase of reaction rates and thus generated heat, which increases the local temperature and exponentially leads to even more heat generation. However, increasing the temperature inside the reactor means that the catalyst effectiveness will decrease due to an exponential increase of reaction rate with temperature. This causes an opposite effect of increasing T_{in} via reduction of heat generation because of lower catalyst effectiveness. For inlet temperatures shown in Fig. 7(b), inlet η_{CO} decreased from 0.53 to 0.27 for T_{in}= 473 and 496 K, respectively. Still, the increase of generated heat due to the increase of reaction rate with inlet temperature surpasses its decrease and eventually ignition temperature is reached (inlet temperature at which thermal runaway occurs). For the base case conditions, the maximum allowable inlet temperature is 496 K. Values above that led to temperature runaways (T=497 in Fig. 7(b)).

However, higher inlet temperatures are possible, but they have to be accompanied by higher velocities, lower T_{wall} or even lower effectiveness factors (e.g., by using larger particles or eggshell catalyst distribution). However, the use of inlet temperatures above 493 K for Co-based FTS catalysts is usually considered unfavorable due to a negative impact on product selectivity (more CH_4 and light hydrocarbons).

For fixed bed operation the coolant temperature is usually set to be equal to the inlet feed temperature or a few degrees below [34]. Fig. 7(c) shows the influence of coolant temperature (wall temperature) on the core temperature along the reactor using the scenario in which runaway would occur due to high inlet temperature (T_{in}=497 K, see Fig. 7(b)). We can see that even relatively minor variations of wall temperature can have a significant effect on the ability of the system to remove generated heat. It is desirable to maintain stable axial temperature profile along the reactor length. Our base case inlet temperature is relatively low (473 K), so T_{wall} does not need to be lower than T_{in} in order to provide needed heat removal. Low values of T_{wall} (e.g. $T_{wall}=T_{in}-5$ K) can even lead to over-cooling, which is not beneficial. However, some situations, e.g., T_{in}>500 K, would require even lower T_{wall} and a stable temperature profile throughout the reactor tube would be difficult to maintain. Jess et al. [19] showed that in most cases $T_{wall}=T_{in}-6$ K is sufficient to go from runaway to stable thermal behavior. Our simulations show that difference can be even lower (2.5-5 K), if the influence of liquid phase on heat transport is taken into account.

The other inlet process conditions which could be changed in FTS are inlet pressure (P_{in}) and H_2/CO feed ratio (FR). These mainly affect heat management characteristics via their effect on catalyst effectiveness and reaction rate, i.e., heat generation. Decrease of FR from 2.2 to 1.8, while keeping other parameters at the base values, results in an increase of the CO effectiveness factor (from 0.49 to 0.58 for reactor inlet), and decrease in FTS reaction rate at the inlet ($(-R_{CO})$ from 24.6 to 20.7 mol/(kg_{cat}·h) for reactor inlet), which have opposite effects on heat generation. In addition, considering that H_2 has a much higher heat capacity and thermal conductivity compared to CO, the decrease of FR also alters the physical properties of syngas mixture, which has an effect on the rate of heat removal. However, the feed composition effect is found to be relatively minor with U=654 and 645 W/(m^2·K) for FR=2.2 and 1.8, respectively. Increasing P_{in} increases both the catalyst effectiveness in terms of CO and FTS reaction rate, which would increase the amount of generated heat. If the inlet molar flowrate remains constant, then increasing pressure will decrease the gas phase velocity, which in turn will have a negative impact on heat removal characteristics. Because both of these process conditions (FR and P_{in}) mainly affect heat management indirectly, through variations of the catalyst effectiveness factor and reaction rate, readers are referred to our recent study on the catalyst particle modeling for more details [50].

5. Effect of Reactor Tube Size and Catalyst Particle Diameter on Temperature Distribution

Several literature studies reported an overall positive effect of increasing particle size (d_p) on the reactor heat management [8,20]. Jess et al. [19,20] discussed the beneficial effect of increasing d_p for a constant tube diameter (d_t). They concluded that even though the catalyst effectiveness is decreased, higher d_p improves the productivity because it improves heat transfer allowing for use of higher temperatures inside the reactor and thus higher conversions. As a result d_p=4 mm was proposed as the optimal size of catalyst particles, despite its very low catalyst effectiveness factor.

A number of simulations were performed using different values of d_p. Because this parameter affects the value of Reynolds numbers, which is shown to have a significant effect on heat transport coefficients (Fig. 8), simulations were done with either keeping the inlet flowrate constant (variable Re) or where Re is kept constant (variable F_{in}). Note that all of the Reynolds numbers used in this paper refer to particle Reynolds numbers ($Re=(\rho u_s d_p/\mu)$. Fig. 9(a) shows the effect of d_p at fixed inlet flowrate on the core temperature along the reactor. Higher particle sizes (d_p=2 and 3 mm) result in lower axial temperature gradients compared to smaller particles (d_p=1 mm). Except for the initial temperature increase close to the reactor inlet, the temperature is almost uniform throughout the reactor (d_p=3 mm and T_{in}=473 K). From the standpoint of heat generation, this is directly related to catalyst effectiveness values,

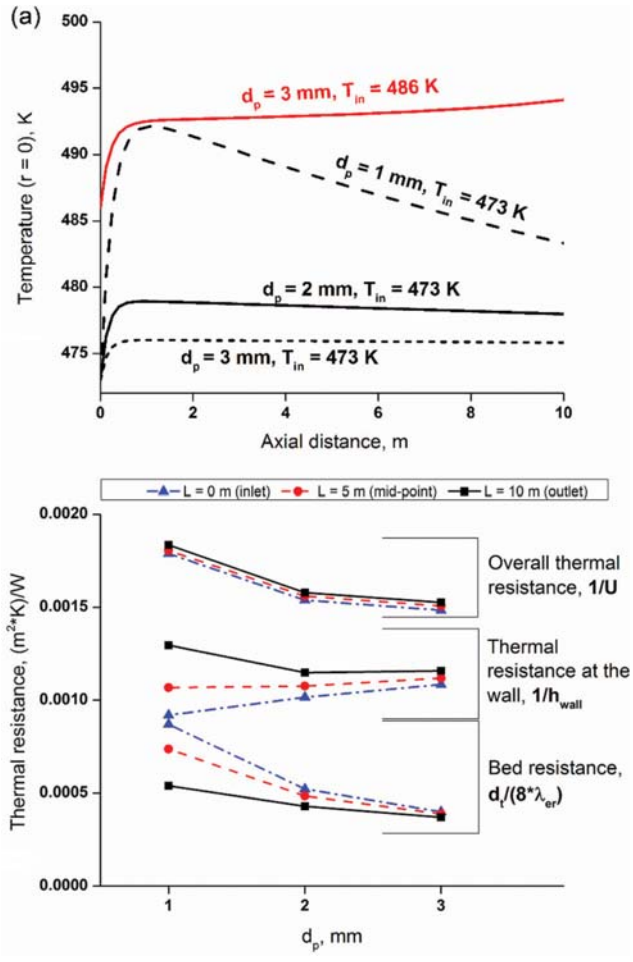

Fig. 9. Effect of varying particle size on heat management: (a) Core temperature along the reactor for d_p=1-3 mm ($T_{wall}=T_{in}$, P_{in}= 2.5 MPa, FR=2, F_{in}=0.150 mol/s, d_t=2.6 cm); (b) overall thermal resistance and its components for d_p=1-3 mm (T_{in}=473 K, $T_{wall}=T_{in}$, P_{in}=2.5 MPa, FR=2, F_{in}=0.150 mol/s, u_s^{in}=0.45 m/s, d_t=2.6 cm).

which goes from 0.91 to 0.31 at inlet conditions for d_p=1 and 3 mm, respectively. The effect on heat removal characteristics is somewhat more complex, but increasing d_p results in the decrease of the overall heat resistance (Fig. 9(b)). Our results at fixed inlet flowrates show that this is related to the decrease in resistance of heat transfer trough the bed, while resistance at the wall remains relatively constant or even increases (based on the inlet and midpoint positions). Interestingly, simulations at fixed Reynolds number at the inlet (variable inlet velocity) show both h_{wall} and λ_{er} decreasing with d_p (simulations with fixed Re are not shown in Figures), which means that the beneficial effect of increasing d_p on heat management is related only to the lower heat generation due to loss of effectiveness and improvements in the overall heat transport via increase of Reynolds numbers.

The utilization of smaller particles results in both higher catalyst effectiveness and average reactor temperatures, and thus in higher conversion level with X_{CO}=58% for d_p=1 mm, compared to X_{CO}=27% for the base case (d_p=2 mm) and X_{CO}=16% for d_p=3 mm. However, improved heat management might allow for increased inlet temperature to compensate for this loss in conversion. If T_{in} is increased from 473 to 486 K for d_p=3 mm, an increase of CO conversion to 38% is observed. However, in this case temperature slowly increases along the reactor and an inflection point appears (red line in Fig. 9(a)). Interestingly, such behavior is indicative of a region of process conditions where thermal behavior is highly sensitive to process condition variations. Further increases of T_{in} beyond 486 K lead to temperature runaways. Therefore, even though there are some heat management benefits to using higher d_p, as well as a decrease in pressure drop, the increase of inlet temperature needed to compensate for the loss of effectiveness with larger particles is necessary, which leads to a much higher sensitivity of the system and potential runaways.

The main drawbacks to utilization of very small particle sizes (d_p<1 mm) are high pressure drops and large axial temperature gradients. The pressure drop with d_p=1 mm for conditions used in Fig. 9(a) is ~0.04 MPa/m, while for d_p=2 mm it is about two-times lower. Further decreases of d_p lead to too high values of pressure drop, which can be counteracted by decreasing the inlet flowrate, but that would lead to poorer heat management (see Section 3.4) and lower productivity. Therefore, the optimal value for the particle size in terms of heat management and productivity seems to be in the recommended 1-3 mm range. Productivity per gram of catalyst can probably also be optimized by utilization of eggshell catalyst distribution or modification of inlet conditions (e.g. use of higher pressures) to increase the catalyst utilization, but this is not directly related to heat management and is outside the scope of the present study.

Increasing the tube size is known to have a negative effect on FTS FBR heat management, and reactors with larger tube sizes are much more likely to suffer from temperature runaways [13]. The range of tube diameter applied commercially in conventional MTF-BRs is 1-2 inch (~2.5-5 cm), where larger tubes are used for Fe and smaller tubes for Co catalysts [8]. A number of model simulations were conducted to study the effect of d_t in the range of 1.5 to 5.9 cm. These included cases with fixed F_{in} (variable inlet superficial velocity) or fixed inlet Reynolds number (constant inlet superficial velocity). Variation of d_t at fixed F_{in}=0.15 mol/s resulted in large changes of velocity inside the reactor, and runaway is observed already at d_t=3.8 cm (superficial inlet gas phase velocity 0.2 m/s). This runaway is a result of a combination of lower values of

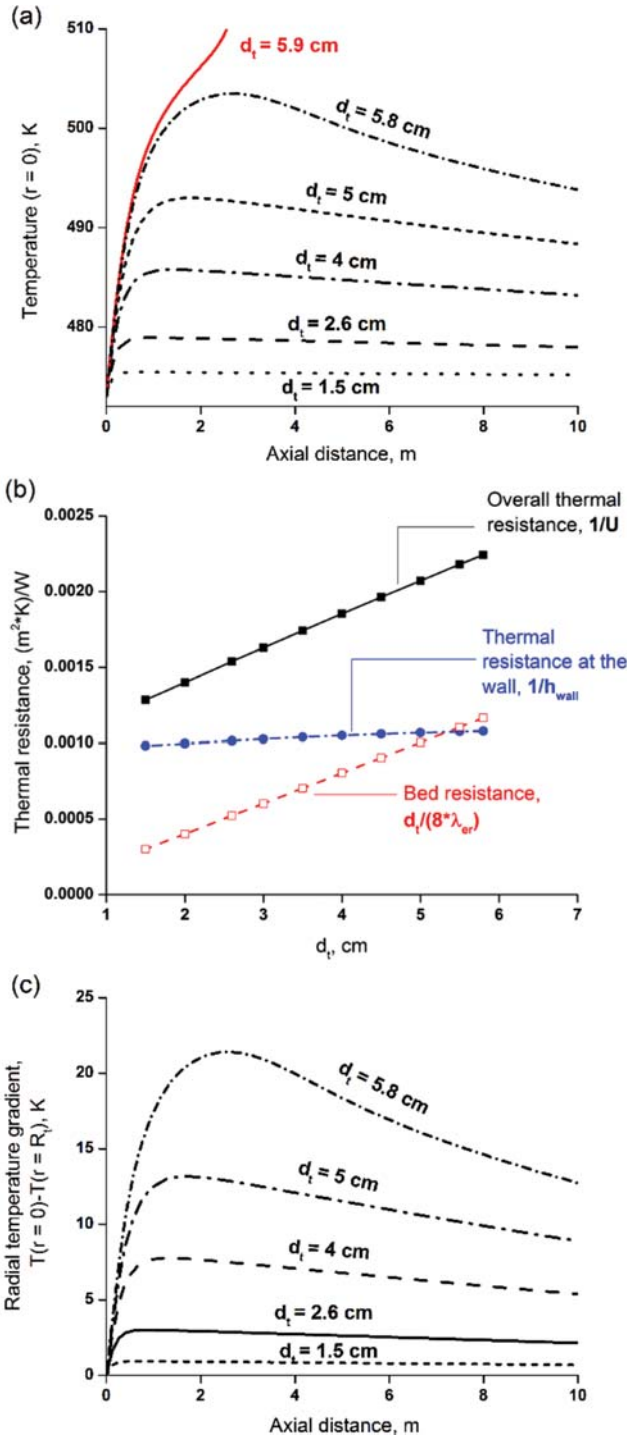

Fig. 10. Effect of varying tube diameter on heat management for d_t=1.5-5.8 cm at fixed Re (T_{in}=473 K, T_{wall}=T_{in}, P_{in}=2.5 MPa, FR=2, F_{in}=0.05-0.752 mol/s, u_s^{in}=0.45 m/s, d_p=2 mm): (a) Core temperature along the reactor; (b) overall thermal resistance and its components at reactor inlet; (c) radial temperature gradient along the reactor.

heat transport coefficients due to decreased velocities and higher radial heat transport resistance due to larger tube size. The former effect can be alleviated by simultaneously increasing inlet flowrate with d_t, thereby increasing reactor throughput. The limits of this approach are tested by simulating increasing d_t at constant inlet Reynolds number (inlet superficial velocity 0.45 m/s). The results of these simulations are presented in Fig. 10. The increase of d_t from 1.5 to 5.8 cm, accompanied with an increase of inlet flowrate from 0.05 to 0.75 mol/s, results in the increase of maximum core temperature from 475 to 503 K (Fig. 10(a)). Conversion level goes from 26.3 to 34.1%, for d_t=1.5-5.8 cm, respectively, meaning a marked increase in productivity per tube is achieved. Further increase of d_t leads to temperature runaway if cooling temperature is not decreased. This is caused by a high increase of radial resistance to heat transport as shown in Fig. 10(b).

Wang et al. [12] also showed that the tube size should be kept below 6 cm; however, their simulations were conducted at T_{in}= 523 K to make up for lower activity of a Fe-based catalyst. Jess et al. [19] study with cobalt fixed the desired conversion level at 27% and decreased inlet temperature (T_{in}=T_{cool}) with increasing tube diameter in order to achieve that level. They concluded that this conversion level cannot be reached without temperature runaway for d_t>39 mm and d_p=3 mm. They suggested d_t=4 cm and d_p=4 mm as optimal values for these two parameters. However, this is predicated on the idea that single-pass conversion has to be maintained below 30%. Depending on other process conditions, mainly water partial pressure, the conversion level can be set higher. Therefore, it is difficult to claim optimal conditions without rigorous mathematical optimization of the system with reasonable physical constraints and objective functions [65]. Our results show that tube diameters as high as 5 cm can be used with relatively constant temperature throughout the reactor. Conversion achieved in this case is about 31.4%. However, this causes a large temperature increase close to the inlet. For d_t=5 cm hotspot temperature is about 493 K, which is already close to the upper limit usable in FTS over cobalt catalyst due to poor selectivity. The axial and radial temperature gradients at the hotspot for d_t=5 cm are 20 and 13 K, respectively. Fig. 10(c) shows the increase of radial temperature gradient, i.e., difference of bed temperature in the core and at the wall, in d_t= 1.5-5.8 cm range. From Figs. 10(a) and 10(c) we can conclude that higher d_t values result in very non-isothermal operating conditions. A benefit of increasing d_t is that it allows for the use of higher F_{in}, thus enabling higher reactor productivity. However, similar benefits can be achieved by scaling-up the number of tubes, while keeping their diameter low. The choice of optimal configuration can only be made by consideration of reactor construction cost and other techno-economic objective functions.

CONCLUSIONS

A two-dimensional pseudo-homogeneous model was developed to simulate the performance of FTS FBR in terms of heat management. The main features of the model are: detailed FTS kinetics for Co-based catalyst, the estimate of catalyst effectiveness factor based on modeling of spherical catalyst pellets and accounting for liquid phase formation and its effect on heat transport.

The influence of several process and design parameters (inlet flowrates and temperature, wall temperature, tube and particle diameter) on temperature distribution in radial and axial direction was investigated. At the base conditions used as reference in this study (T_{in}=473 K, P_{in}=25 bar, H_2/CO feed ratio=2, F_{in}=0.15 mol/s, u_s^{in}= 0.45 m/s, T_{wall}=T_{in}, d_t=2.6 cm, d_p=2 mm, L=10 m) temperature increases in axial direction and reaches a maximum value in the reactor tube core of 479 K close to the inlet (z~1 m), after which it decreases gradually along the reactor. The radial gradient inside the tube is about 3 K at the maximum temperature position. Comparison with equivalent one-dimensional model shows a very small difference in terms of predictions of the overall CO conversion and C_{5+} productivity. This difference becomes more significant for larger tube diameters, making the two-dimensional approach necessary to obtain the correct results. Accounting for effectiveness factor changes with process parameters has been shown to be of paramount importance in predicting the thermal behavior.

Simulations with varying one process or design parameter and keeping others constant at the base case values show temperature runaway occurring for F_{in}<0.03 mol/s (inlet velocity 0.09 m/s), T_{in}>497 K and d_t>5.9 cm. Thermal behavior is a complex function of process conditions, and often a variation of one parameter can have opposite influences (both positive and negative effects) on heat management. For example, increasing the inlet temperature increases the reaction rate and thus amount of generated heat. However, it also decreases the catalyst effectiveness, which results in a lower heat generation.

Varying the inlet flowrate shows that the gas phase velocity increase has a strong positive effect on the heat transfer coefficient at the wall; however, the impact of gas phase composition is noticeable as well. The highest h_{wall} values are achieved with pure syngas (inlet conditions), while generation of hydrocarbons along the reactor (X_{CO}>0%) changes the physical properties of the gas phase and results in h_{wall} decrease. Increase in the gas phase velocity also has a positive effect on the effective radial thermal conductivity. However, we also see a positive influence of the liquid phase velocity. The liquid phase is generated along the reactor and thus Reynolds number of liquid increases from 0 to 0.57 for the base case inlet and outlet conditions, respectively, resulting in about 20% increase of radial thermal conductivity (λ_{er}).

The increase of particle diameter is beneficial from the standpoint of heat management, both from the perspective of decreased heat generation due to lower effectiveness factor and higher heat transport coefficients due to increased Reynolds numbers. However, this leads to low productivity and poor FTS product selectivity. Tube diameter is a critical parameter in terms of FBR heat management and radial temperature gradients of 20 K or higher were observed in simulations (d_t>5.8 cm). The increase of tube diameter results in much higher hotspots and more likely runaways, due to higher radial thermal resistance and lower transport coefficients related to lower gas and liquid velocities. These adverse effects can be somewhat alleviated by increasing the F_{in} or lowering T_{in} or T_{wall}, but not completely avoided.

Simulation results with the variation of process and design parameters show that FTS FBRs are very sensitive in terms of heat management and any large disturbance can lead to potential temperature

runaway. Therefore, special care has to be given to heat management issues when designing an FBR for FTS. Due to many conflicting effects between heat management constraints and desire for higher productivity, as well as their sensitivity, optimization of all relevant parameters for a given catalyst is necessary to achieve the optimal reactor performance.

SUPPORTING INFORMATION

Equations for calculation of reaction kinetics and kinetic parameters (Eqs. (S.1)-(S.23), Table S1), parameters used for calculation of heat of reaction (Table S2), effective radial diffusivity (Eq. (S.24)), estimation of liquid flowrate (Eqs. (25)-(34)), effective intraparticle diffusivity (Eqs. (S35)-(39)), gas and liquid phase physical properties (Table S3), miscellaneous parameters and relations (Eqs. (40)-(51)) and solution initialization procedure.

Additional information as noted in the text. This information is available via the Internet at http://www.springer.com/chemistry/journal/11814.

ACKNOWLEDGEMENTS

This research was made possible by NPRP grants 7 - 559 - 2 - 211 from the Qatar National Research Fund (a member of Qatar Foundation). The statements made herein are solely the responsibility of the authors.

NOMENCLATURE

A_{cs} : tube cross-section area [m^2]
Bi : Biot number pdimensionless]
C_i : molar concentration of component i [mol/m^3]
C_{CO}^S : molar liquid phase concentration of CO at the surface of the catalyst particle [mol/m^3]
C_p : fluid heat capacity [J/(kg·K)]
ΔC_p : overall change in heat capacity per mole of CO [J/(kg·K)]
D_i^{er} : effective radial diffusivity of species i [m^2/s]
$D_{e,CO}$: effective intraparticle diffusivity of CO in wax [m^2/s]
d_t : tube diameter [m]
d_p : particle diameter [m]
f : friction factor for fluid flow in a packed bed [dimensionless]
F_{in} : inlet flowrate [mol/s]
FR : H_2/CO feed ratio [dimensionless]
H_f^θ : standard enthalpy of formation [J/mol]
ΔH_r : reaction enthalpy per mole of CO consumed [J/mol]
ΔH_r^θ : standard reaction enthalpy per mole of CO consumed [J/mol]
h_{wall} : radial heat transfer coefficient at the wall [$W/(m^2 \cdot K)$]
L : tube length [m]
P_{in} : inlet pressure [Pa]
Pr : Prandtl number [dimensionless]
P_t : total pressure [Pa]
r : radial distance [m]
Re : Reynolds number [dimensionless]
R_i : rate of species i disappearance or formation [$mol/(kg_{cat} \cdot s)$]
R_t : tube radius [m]
r_p : particle radius [m]
T : temperature [K]
$T_{ave}(z)$: average cross-section temperature [K]
T_{cool} : coolant temperature [K]
T_{in} : inlet temperature [K]
T^θ : standard temperature [K]
T_{wall} : wall temperature [K]
U : overall heat transport coefficient [$W/(m^2 \cdot K)$]
u_s : superficial fluid velocity [m/s]
z : axial distance [m]

Greek Letters

$(\alpha\beta)$: coefficients of Matsuura et al. correlation [dimensionless]
δ : catalyst layer thickness [μm]
η_i : catalyst effectiveness for species i [dimensionless]
θ : standard
λ_{er} : effective radial thermal conductivity [W/(m·K)]
ρ : fluid density [kg/m^3]
ρ_b : bed density [kg/m^3]
ρ_p : particle density [kg/m^3]
ϕ : generalized Thiele modulus [dimensionless]

Subscripts and Superscripts

g : gas phase
l : liquid phase
in : inlet
i : component (i=CO, H_2, H_2O and C_nH_m)

REFERENCES

1. M. E. Dry and A. P. Steynberg, *Chapter 5 - Commercial FT Process Applications, Studies in Surface Science and Catalysis*, Elsevier, **152**, 406 (2004).
2. S. T. Sie, M. M. G. Senden and H. M. H. Van Wechem, *Catal. Today*, **8**(3), 371 (1991).
3. A. Hoek and L. B. J. M. Kersten, The Shell Middle Distillate Synthesis process: technology, products and perspective, *Studies in Surface Science and Catalysis*, Elsevier, **147**, 25 (2004).
4. A. Jess, R. Popp and K. Hedden, *Appl. Catal. A*, **186**, 321 (1999).
5. D. Bode and S. T. Sie, US Patent US4686238 A (1987).
6. S. T. Sie and R. Krishna, *Appl. Catal. A*, **186**, 55 (1999).
7. A. Y. Khodakov, W. Chu and P. Fongarland, *Chem. Rev.*, **107**, 1692 (2007).
8. A. P. Steynberg, M. E. Dry, B. H. Davis and B. B. Breman, Chapter 2 - Fischer-Tropsch Reactors, *Studies in Surface Science and Catalysis*, Elsevier, **152**, 64 (2004).
9. O. M. Basha, L. Sehabiague, A. Abdel-Wahab and B. I. Morsi, *Int. J. Chem. Reactor Eng.*, **13**(3), 201 (2015).
10. H. E. Atwood and C. O. Bennett, *Ind. Eng. Chem. Process Des. Dev.*, **18**, 163 (1979).
11. G. Bub and M. Baerns, *Chem. Eng. Sci.*, **35**, 348 (1980).
12. Y.-N. Wang, Y.-Y. Xu, Y.-W. Li, Y.-L. Zhao and B.-J. Zhang, *Chem. Eng. Sci.*, **58**, 867 (2003).
13. G. Chabot, R. Guilet, P. Cognet and C. Gourdon, *Chem. Eng. Sci.*, **127**, 72 (2015).
14. R. Guettel and T. Turek, *Chem. Eng. Sci.*, **64**, 955 (2009).

15. K. M. Brunner, J. C. Duncan, L. D. Harrison, K. E. Pratt, R. P. S. Peguin, C. H. Bartholomew and W. C. Hecker, *Int. J. Chem. Reactor Eng.*, **10**, 1 (2012).
16. A. Sharma, R. Philippe, F. Luck and D. Schweich, *Chem. Eng. Sci.*, **66**, 6358 (2011).
17. T. S. Lee and J. N. Chung, *Energy Fuels*, **26**, 1363 (2012).
18. A. Jess and C. Kern, *Chem. Eng. Technol.*, **32**, 1164 (2009).
19. A. Jess and C. Kern, *Chem. Eng. Technol.*, **35**(2), 369 (2012).
20. A. Jess and C. Kern, *Chem. Eng. Technol.*, **35**, 379 (2012).
21. A. Moutsoglou and P. P. Sunkara, *Energy Fuels*, **25**(5), 2242 (2011).
22. M. M. Ghouri, S. Afzal, R. Hussain, J. Blank, D. B. Bukur and N. O. Elbashir, *Comput. Chem. Eng.*, **91**, 38 (2016).
23. N. Park, J. R. Kim, Y. Yoo, J. Lee and M. J. Park, *Fuel*, **122**, 229 (2014).
24. P. Kaiser and A. Jess, *Energy Technol.*, **2**(5), 486 (2014).
25. A. Ghareghashi, F. Shahraki, K. Razzaghi, S. Ghader and M. A. Torangi, *Korean J. Chem. Eng.*, **34**, 87 (2017).
26. J. Knochen, R. Guettel, C. Knobloch and T. Turek, *Chem. Eng. Process.*, **49**, 958 (2010).
27. M. Stamenić, V. Dikić, M. Mandić, B. Todić, D. B. Bukur and N. M. Nikačević, *Ind. Eng. Chem. Res.*, **56**(36), 9964 (2017).
28. N. J. Mariani, O. M. Martínez and G. F. Barreto, *Chem. Eng. Sci.*, **56**(21-22), 5995 (2001).
29. A. M. Hilmen, E. Bergene, O. A. Lindvåg, D. Schanke, S. Eri and A. Holmen, *Catal. Today*, **105**(3-4), 357 (2005).
30. R. M. de Deugd, F. Kapteijn and J. A. Moulijn, *Catal Today*, **79-80**, 495 (2003).
31. A. Matsuura, Y. Hitaka, T. Akehata and T. Shirai, *Heat Transfer - Jpn. Res.*, **8**, 44 (1979).
32. M. R. Khadilkar, PhD Thesis, Washington University (1998).
33. M. F. M. Post, A. C. Van't Hoog, J. K. Minderhoud and S. T. Sie, *AIChE J.*, **35**(7), 1107 (1989).
34. G. F. Froment, K. B. Bischoff and J. De Wilde, *Chemical Reactor Analysis and Design*, 3rd Ed., Wiley (2011).
35. L. C. Young and B. A. Finlayson, *Ind. Eng. Chem. Fund.*, **12**, 412 (1973).
36. A. de Klerk, *AIChE J.*, **49**, 2022 (2003).
37. H. Delmas and G. F. Froment, *Chem. Eng. Sci.*, **43**, 2281 (1988).
38. B. Todic, T. Bhatelia, G. F. Froment, W. Ma, G. Jacobs, B. H. Davis and D. B. Bukur, *Ind. Eng. Chem. Res.*, **52**, 669 (2013).
39. I. C. Yates and C. N. Satterfield, *Energy Fuels*, **5**(1), 168 (1991).
40. W. Ma, G. Jacobs, T. K. Das and B. H. Davis, *Ind. Eng. Chem. Res.*, **53**(6), 2157 (2014).
41. B. Todic, W. Ma, G. Jacobs, B. H. Davis and D. B. Bukur, *Catal. Today*, **228**, 32 (2014).
42. S. Ergun, *Chem. Eng. Prog.*, **48**, 89 (1952).
43. R. Krishna and S. T. Sie, *Chem. Eng. Sci.*, **49**, 4029 (1994).
44. W. H. Zimmerman, J. A. Rossin and D. B. Bukur, *Ind. Eng. Chem. Res.*, **28**(4), 406 (1989).
45. M. E. Dry, *Appl. Catal. A.*, **138**(2), 319 (1996).
46. B. Kaskes, D. Vervloet, F. Kapteijn and J. R. van Ommen, *Chem. Eng. J.*, **283**, 1465 (2016).
47. H. S. Fogler, *Elements of chemical reaction engineering*, Prentice-Hall (1992).
48. B. Poling, J. Prausnitz and J. O. Connell, *The Properties of Gases and Liquids*, McGraw-Hill Education (2000).
49. P. Chaumette, C. Verdon and P. Boucot, *Top. Catal.*, **2**(1-4), 301 (1995).
50. M. Mandić, B. Todić, L. Živanić, N. Nikačević and D. B. Bukur, *Ind. Eng. Chem. Res.*, **56**(10), 2733 (2017).
51. C. Erkey, J. B. Rodden and A. Akgerman, *Can. J. Chem. Eng.*, **68**, 661 (1990).
52. J. J. Marano and G. D. Holder, *Fluid Phase Equilib.*, **138**, 1 (1997).
53. A. P. de Wasch and G. F. Froment, *Chem. Eng. Sci.*, **27**(3), 567 (1972).
54. C.-H. Li and B. Finlayson, *Chem. Eng. Sci.*, **32**(9), 1055 (1977).
55. V. Specchia, G. Baldi and S. Sicardi, *Chem. Eng. Commun.*, **4**, 361 (1980).
56. Y. Demirel, R. Sharma and H. Al-Ali, *Int. J. Heat Mass Transfer.*, **43**(2), 327 (2000).
57. O. Bey and G. Eigenberger, *Int. J. Therm. Sci.*, **40**(2), 152 (2001).
58. S. Yagi and D. Kunii, *AIChE J.*, **6**(1), 97 (1960).
59. P. H. Calderbank and L. A. Pogorski, *Trans. Inst. Chem. Eng.*, **35**, 195 (1957).
60. M. J. Taulamet, N. J. Mariani, G. F. Barreto and O. M. Martínez, *Rev. Chem. Eng.*, **31**, 97 (2015).
61. A. Matsuura, Y. Hitaka, T. Akehata and T. Shirai, *Heat Transfer - Jpn. Res.*, **8**, 53 (1979).
62. Y.-N. Wang, W.-P. Ma and Y.-J. Lu, *Fuel*, **82**(2), 195 (2003).
63. S. T. Sie and R. Krishna, *Appl. Catal. A.*, **186**, 55 (1999).
64. V. Hlavacek, *Ind. Eng. Chem.*, **62**, 8 (1970).
65. K. Ghodasara, R. Smith and S. Hwang, *Korean J. Chem. Eng.*, **31**, 1136 (2014).

Supporting Information

Effects of process and design parameters on heat management in fixed bed Fischer-Tropsch synthesis reactor

Branislav Todic*,†, Milos Mandic*, Nikola Nikacevic, and Dragomir B. Bukur*,***,†**

*Chemical Engineering Program, Texas A&M University at Qatar, P. O. Box 23874, Doha, Qatar
**Faculty of Technology and Metallurgy, University of Belgrade, Karnegijeva 4, Belgrade, Serbia
***Texas A&M University, 3122 TAMU, College Station, Texas 77843, United States
(*Received 8 October 2017 • accepted 1 December 2017*)

This section provides all relevant model equations that were left out of the main text due to limited space available.

REACTION KINETICS

The CO disappearance rate is calculated according to Yates-Satterfield model [1]:

$$(-R_{CO})=\frac{k\cdot P_{CO}\cdot P_{H_2}}{(1+a\cdot P_{CO})^2} \tag{S.1}$$

where $(-R_{CO})$ is the rate of CO disappearance; P_{CO}, P_{H_2}, P_{H_2O} are partial pressures of CO, H_2 and H_2O; k, a are kinetic parameters. Kinetic parameters in Eq. (S.1) are estimated for 0.48%Re-25%Co/Al_2O_3 CAER catalyst as [2]:

$$k=1.52*10^8 e^{\frac{72.69*10^3}{8.314*T}} \tag{S.2}$$

$$a=0.645 e^{\frac{10.77*10^3}{8.314*T}} \tag{S.3}$$

The H_2 consumption rate and H_2O formation rate are defined by:

$$(-R_{H_2})=UR\times(-R_{CO}) \tag{S.4}$$

$$(R_{H_2O})=(-R_{CO}) \tag{S.5}$$

where UR is the H_2/CO usage ratio, which depends on selectivity as explained below.

Product selectivity calculations for methane and C_{2+} hydrocarbons utilize kinetic models of Ma et al. [3] and Todic et al. [4], respectively. Both of the models provide rate expressions for product species, but these rates have to be normalized with respect to Yates-Satterfield CO consumption rate in order to maintain C-, H- and O-atomic closures.

Ma et al. model [3] provides the following equation for methane formation rate:

$$R_{CH_4}^{Ma}=\frac{k_M\cdot P_{CO}^{a_M}\cdot P_{H_2}^{b_M}}{\left(1+m_M\cdot\frac{P_{H_2O}}{P_{H_2}}\right)} \tag{S.6}$$

where R_{CH_4} is rate of methane formation; k_M, a_M, b_M and m_M are kinetic parameters. Kinetic parameters in Eq. (S.7) were estimated for 0.48%Re-25%Co/Al_2O_3 catalyst and are presented in Ref. [2]:

$$k_M=1.57*10^{12} e^{\frac{139.98*10^3}{8.314*T}} \tag{S.7}$$

$$a_M=-0.99 \tag{S.8}$$

$$b_M=1.28 \tag{S.9}$$

$$m_M=0.58 \tag{S.10}$$

According to Todic et al. detailed kinetic model [4] the rates of C_{2+} product formation can be calculated as:

$$R_{C_nH_{2n+2}}^{det}=k_7K_2^{0.5}P_{H_2}^{0.5}\alpha_1\alpha_2\prod_{i=3}^{n}\alpha_i\cdot[S]^2 \qquad n\geq 2 \tag{S.11}$$

$$R_{C_2H_4}^{det}=k_{8E,0}e^{c\cdot 2}\alpha_1\alpha_2\cdot[S] \tag{S.12}$$

$$R_{C_nH_{2n}}^{det}=k_{8,0}e^{c\cdot n}\alpha_1\alpha_2\prod_{i=3}^{n}\alpha_i\cdot[S] \qquad n\geq 3 \tag{S.13}$$

where the left-hand side of equations represents rates of formation of C_{2+} n-paraffin, ethene and C_{3+} 1-olefin. Rates are described using kinetic rate constants (k's) and equilibrium constants (K's), partial pressures (P_i's), chain growth probabilities (α's) and fraction of vacant sites [S]. The chain growth probabilities and [S] are calculated as:

$$\alpha_1=\frac{k_3K_1P_{CO}}{k_3K_1P_{CO}+k_{7M}\sqrt{K_2P_{H_2}}} \tag{S.14}$$

$$\alpha_2=\frac{k_3K_1P_{CO}[S]}{k_3K_1P_{CO}[S]+k_7\sqrt{K_2P_{H_2}}[S]+k_{8,E}e^{c\cdot 2}} \tag{S.15}$$

$$\alpha_n=\frac{k_3K_1P_{CO}[S]}{k_3K_1P_{CO}[S]+k_7\sqrt{K_2P_{H_2}}[S]+k_{8,0}e^{c\cdot n}} \qquad n\geq 3 \tag{S.16}$$

$$[S]=1/\left\{1+K_1P_{CO}+\sqrt{K_2P_{H_2}}+\left(\frac{1}{K_2^2K_4K_5K_2}\frac{P_{H_2O}}{P_{H_2}^2}+\sqrt{K_2P_{H_2}}\right)\cdot\left(\alpha_1+\alpha_1\alpha_2+\alpha_1\alpha_2\sum_{i=3}^{n}\prod_{j=3}^{i}\alpha_j\right)\right\} \tag{S.17}$$

Kinetic parameters used in Eqs. (S.12)-(S.18) are estimated for

Table S1. Parameters of Todic et al. [4] detailed kinetic model used in calculation of C_{2+} n-paraffin and 1-olefin formation rates

Parameter	Value	Unit	Parameter	Value	Unit
A_1	$6.59*10^{-5}$	MPa-1	ΔH_1	−48.9	kJ/mol
A_2	$1.64*10^{-4}$	MPa-1	ΔH_2	−9.4	kJ/mol
A_3	$4.14*10^{8}$	mol/(g_{cat}*h)	E_3	92.8	kJ/mol
A_4	$3.59*10^{5}$	-	ΔH_4	16.2	kJ/mol
A_5	$9.81*10^{-2}$	-	ΔH_5	11.9	kJ/mol
A_6	$1.59*10^{6}$	MPa	ΔH_6	14.5	kJ/mol
A_7	$4.53*10^{7}$	mol/(g_{cat}*h)	E_7	75.5	kJ/mol
A_8	$4.11*10^{8}$	mol/(g_{cat}*h)	E_8	100.4	kJ/mol
A_{7M}	$7.35*10^{7}$	mol/(g_{cat}*h)	E_{7M}	65.4	kJ/mol
A_{8E}	$4.60*10^{7}$	mol/(g_{cat}*h)	E_{8E}	103.2	kJ/mol
ΔE	1.1	kJ/mol/CH_2			

the same 0.48%Re-25%Co/Al_2O_3 catalyst and are presented in Table S1. The amount of CO and H_2 needed to form these products is then:

$$(-R_{CO})^{prod} = R_{CH_4}^{Ma} + \sum_{n=2}^{57} n \times (R_{C_nH_{2n+2}}^{det} + R_{C_nH_{2n}}^{det}) \quad \text{(S.18)}$$

$$(-R_{H_2})^{prod} = 3 \times R_{CH_4}^{Ma} + \sum_{n=2}^{52} [(2n+1) \times R_{C_nH_{2n+2}}^{det} + 2n \times R_{C_nH_{2n}}^{det}] \quad \text{(S.19)}$$

Based on this we can also get the usage ratio and normalized CH_4, C_2, C_3, … C_{24} and lumped C_{25+} product formation rates:

$$UR = (-R_{H_2})^{prod} / (-R_{CO})^{prod} \quad \text{(S.20)}$$

$$R_{CH_4} = \frac{R_{CH_4}^{Ma}}{(-R_{CO})^{prod}} (-R_{CO}) \quad \text{(S.21)}$$

$$R_{C_n} = \frac{R_{C_nH_{2n+2}}^{det} + R_{C_nH_{2n}}^{det}}{(-R_{CO})^{prod}} (-R_{CO}) \qquad 2 \le n \le 24 \quad \text{(S.22)}$$

$$R_{C_{25+}} = \frac{\sum_{n=25}^{57} (R_{C_nH_{2n+2}}^{det} + R_{C_nH_{2n}}^{det})}{(-R_{CO})^{prod}} (-R_{CO}) \qquad 25 \le n \le 57 \quad \text{(S.23)}$$

HEAT OF REACTION

Table S2 gives the parameters used in calculation of heat of reaction.

Table S2. Formation enthalpies, standard reaction enthalpies, heat capacity and overall change in heat capacity for species involved in FTS reaction. Data obtained from Ref. [5] for T=473 K

Species	H_f^θ (kJ/mol)	ΔH_r^θ (kJ/mol)	ΔH_r^θ (kJ/mol CO)	C_p (J/mol·K)	ΔC_p (J/mol CO·K)
H_2	0.0	-	-	29.3	-
CO	−110.5	-	-	29.8	-
H_2O	−241.8	-	-	35.1	-
CH_4	−74.5	−205.8	−205.8	44.8	−37.8
C_2H_6	−83.8	−346.4	−173.2	74.4	−30.7
C_3H_8	−104.7	−498.5	−166.2	107.3	−27.3
C_4H_{10}	−125.8	−650.9	−162.7	142.0	−25.1
C_5H_{12}	−146.8	−803.2	−160.6	174.2	−24.3
C_6H_{14}	−166.9	−954.6	−159.1	207.3	−23.6
C_8H_{18}	−208.8	−1259.0	−157.4	273.6	−22.8
$C_{10}H_{22}$	−249.5	−1562.3	−156.2	340.1	−22.2
$C_{15}H_{32}$	−352.7	−2321.9	−154.8	507.0	−21.5
$C_{20}H_{42}$	−455.8	−3081.4	−154.1	673.5	−21.1
C_2H_4	52.5	−210.1	−105.0	59.6	−38.1
C_3H_6	20.0	−373.8	−124.6	91.0	−32.7
C_4H_8	−0.5	−525.7	−131.4	123.2	−29.8
C_5H_{10}	−21.3	−677.7	−135.5	156.7	−27.8
C_6H_{12}	−42.0	−829.6	−138.3	190.0	−26.5
C_8H_{16}	−83.6	−1133.8	−141.7	256.5	−24.9
$C_{10}H_{20}$	−124.2	−1437.0	−143.7	323.1	−23.9

EFFECTIVE RADIAL DIFFUSIVITY (D_i^{er})

Effective radial diffusion contains the contributions of molecular diffusion and convective transport of mass in the radial direction due to irregular pathways within the bed of particles. Considering that vast majority of transport (~99 mol% of components are in gas phase) occurs via gas phase, only the gas phase radial diffusion is taken into consideration for the 2-D material balance. Therefore, D_{er} is calculated for components in the gas phase.

Several authors proposed correlations for this parameter, most of which take into consideration velocity and reactor geometry (d_p and d_t) [6-8]. In our study a correlation proposed by Delmas and Froment [6] was used:

$$\frac{D_{er}}{u_s d_p} = \frac{1}{10}\left[1+19.4\left(\frac{d_p}{d_t}\right)^2\right] \tag{S.24}$$

It is worth nothing that other correlations result in similar values of D_{er} [7,8].

ESTIMATION OF LIQUID FLOWRATE

The split between the gas- and the liquid-phase is estimated along the reactor from vapor-liquid equilibrium (VLE) flash calculations utilizing Raoult's law. This approach was shown to be adequate in representing the VLE of FTS hydrocarbons by Masuku et al. [9].

The required input values for flash calculation are molar fraction of component i (z_i) and its equilibrium constant (K_i). Molar fraction is calculated from the material balance, based on molar flowrate of component i (F_i) and total molar flowrate ($F_{tot}=\sum_i F_i$), as:

$$z_i = \frac{F_i}{F_{tot}} \tag{S.25}$$

The equilibrium constant can be calculated from the Raoult's law:

$$K_i = \frac{P_i^{vap}}{P} \tag{S.26}$$

The vapor pressure correlation for hydrocarbon components was taken from Caldwell and van Vuuren [10]:

$$P_n^{vap} = P_0 \cdot \beta^n \tag{S.27}$$

where:

$$P_0 = 17838.2 \text{ (kPa)} \tag{S.28}$$

$$\beta = \exp\left(-427.218\left(\frac{1}{T}-0.001029807\right)\right) \tag{S.29}$$

where T is in K.

The vapor pressures of non-organic species (CO, H_2 and H_2O) are calculated using the Antoine correlation:

$$\log_{10}(P_i^{vap}) = A - \frac{B}{C+T} \tag{S.30}$$

Where parameters A, B and C are taken from the literature [11].

The compositions of the gas and the liquid phase are then calculated as:

$$x_i = \frac{z_i}{1+x_G(K_i-1)} \tag{S.31}$$

$$y_i = K_i \cdot x_i \tag{S.32}$$

where the fraction of the gas phase in the total flow of mixture (x_G) is the only unknown. The value x_G is found between 0 and 1 by numerically solving the system of Eqs. (S.31) and (S.32) so that $F_x = \sum_{i=CO,\,H_2\ldots}^{C_{57}} x_i - 1 = 0$ and $F_y = \sum_{i=CO,\,H_2\ldots}^{C_{57}} y_i - 1 = 0$. A convenient objective function minimized by varying x_G is [12]:

$$F = F_y - F_x = 0 \tag{S.33}$$

Typical solution for FTS conditions shows $0.99<x_G<1$, meaning that less than 1% of total molar flowrate is in the liquid phase. The flowrate of liquid-phase can be calculated as:

$$F_l = (1-x_G)\cdot F_{tot} \tag{S.34}$$

EFFECTIVE INTRAPARTICLE DIFFUSIVITY

The effective intraparticle diffusion of CO in wax is calculated as:

$$D_{e,\,CO} = D_{wax,\,CO}\frac{\varepsilon_p}{\tau_p} \tag{S.35}$$

where ε_p and τ_p are particle porosity and tortuosity (assumed values are $\varepsilon_p=0.5$ and $\tau_p=2$ [2]) and $D_{wax,\,CO}$ is the diffusivity coefficient of CO in FTS wax (where wax is assumed to be equivalent to n-octacosane). $D_{wax,\,CO}$ is calculated from Akgerman's correlation [9]:

$$D_{wax,\,CO} = \frac{94.5\cdot 10^{-9}\sqrt{T}}{M_{CO}^{0.239} M_{wax}^{0.781} (\sigma_{CO}\sigma_{wax})^{1.134}}(V_b - bV_0) \tag{S.36}$$

using the following parameters: M_{CO}=28.01 g/mol, M_{wax}=394.77 g/mol, σ_{CO}=3.72 Å, σ_{wax}=9.76 Å, $V_b=M_{wax}/\rho_{wax}$, $V_0=N_A(\sigma_{wax}\cdot 10^{-8})3/\sqrt{2}$=396.07 cm^3/mol, $b=1.206+0.0632(\sigma_{CO}/\sigma_{wax})$=1.23.

The concentration of CO in the liquid phase at the catalyst particle surface can be related to the partial pressure of CO at the surface by equation S.37. It is assumed that external mass transport limitations are negligible, so that the CO partial pressure at the surface is equal to the partial pressure in the reactor bulk.

$$P_{CO}^s = H_{CO}(C_{CO}^S/C_{wax}) \tag{S.37}$$

where H_{CO} and C_{wax} are Henry's law constant for CO and total liquid wax concentration ($C_{wax}=\rho_{wax}/M_{wax}$). The Henry's law constant for CO is calculated from correlations provided by Marano and Holder [13]:

$$H_{CO} = \exp(H_{CO,0} - 28\cdot\Delta H_{CO})/(C_{wax}\cdot 10^5) \tag{S.38}$$

$$H_{CO,0} = A + B/T + C\ln T + DT^2 + E/T^2 \tag{S.39}$$

where numerical values of the parameters are: ΔH_{CO}=0.0173238, A=5.79833, B=19.5937, C=0.152199, D=−1.89733*10^{-6}, E=2031.63.

PHYSICAL PROPERTIES

Physical properties of the gas- and the liquid-phase were ob-

Table S3. Values of physical properties provided by Multiflash database for representative reactor positions for base case simulation (T_{in}=473 K, T_{wall}=T_{in}, d_p=2 mm, d_t=2.6 cm, P_{in}=2.5 MPa, feed H_2/CO ratio (FR)=2, F_{in}=0.15 mol/s)

	Physical properties							
Reactor position	ρ_G (kg/m^3)	ρ_L (kg/m^3)	λ_G (W/(m*K))	λ_L (W/(m*K))	μ_G (Pa*s)	μ_L (Pa*s)	$C_{p,G}$ (kJ/(kg*K))	$C_{p,L}$ (kJ/(kg*K))
Inlet X_{CO}=0%	6.79	699	0.113	0.132	2.04E-05	1.02E-03	2.75	2.75
Middle X_{CO}=14%	7.06	695	0.106	0.131	2.01E-05	9.67E-04	2.66	2.77
Outlet X_{CO}=28%	7.47	695	0.097	0.131	1.95E-05	9.72E-04	2.57	2.78

tained from Multiflash database (add-on for gPROMS software package) [14]. The gas-phase was assumed to be comprised of the following components: CO, H_2, H_2O and hydrocarbons CH_4, C_2, … C_{24} and lumped C_{25+}; where hydrocarbons have properties corresponding to those of equivalent n-paraffin. The liquid-phase was assumed to have properties equivalent to those of C_{30} n-paraffin. Physical properties are calculated for each axial point along the reactor as a function of local temperature, pressure and composition. Some representative values of physical properties of the two phases are given in Table S3.

MISCELLANEOUS PARAMETERS AND RELATIONS

Bed porosity [15]:

$$\varepsilon_b = 0.1504 + \frac{0.2024}{\phi_p} + \frac{1.0814}{\left(\frac{d_t}{d_p} + 0.1226\right)^2} \quad \text{(S.40)}$$

where ϕ_p=1 for spherical particles.

Bed (bulk) density was calculated as:

$$\rho_b = \rho_p(1-\varepsilon_b) \quad \text{(S.41)}$$

where ρ_p=1200 kg/m^3 (typical value for Co-based catalysts).

Dimensionless groups are:

$$Re_g = \frac{\rho_g u_{s,g} d_p}{\mu_g} \quad \text{(S.42)}$$

$$Pr_g = \frac{C_{p,g}\mu_g}{\lambda_g} \quad \text{(S.43)}$$

$$Re_l = \frac{\rho_l u_{s,l} d_p}{\mu_l} \quad \text{(S.44)}$$

$$Pr_l = \frac{C_{p,l}\mu_l}{\lambda_l} \quad \text{(S.45)}$$

and velocities are calculated as:

$$u_{s,g} = \frac{F_g M_{g,ave}}{\rho_g A_{cs}} \quad \text{(S.46)}$$

$$u_{s,l} = \frac{F_l M_l}{\rho_l A_{cs}} \quad \text{(S.47)}$$

Because x_G>0.99 for all conditions tested, it can be assumed that u_s=$u_{s,g}$.

Parameters used in calculation of the effective radial thermal conductivity have been fitted to the experimental data of Matsuura et al. [16] using the following dependencies:

$$(\alpha\beta)_g = 9.6\cdot10^3\cdot d_p^2 - 92.3\cdot d_p + 0.51 \quad \text{(S.48)}$$

$$(\alpha\beta)_l = a_{gl}(1+b_{gl}\cdot Re_g) \quad \text{(S.49)}$$

$$a_{gl} = 5.0\cdot10^3\cdot d_p^2 - 43.2\cdot d_p + 0.25 \quad \text{(S.50)}$$

$$b_{gl} = 2.1\cdot10^3\cdot d_p^2 - 18.6\cdot d_p + 0.05 \quad \text{(S.51)}$$

SOLUTION INITIALIZATION PROCEDURE

In order to solve a model of this complexity, gPROMS software requires an initialization procedure. This is done by solving simplified model equations and then using these values as the initial guess for more complex model equations. Following steps have been applied:

1) Solution of isothermal and isobaric model (i.e. mass balance only) with fixed values of physical properties, phase split and kinetic parameters [S] and α_n.

2) All kinetic parameters are calculated. Other eqs. are the same as in Step 1.

3) Physical properties are calculated along the reactor. Other eqs. are the same as in Step 2.

4) VLE flash calculations are performed. Other eqs. are the same as in Step 3.

5) Heat balance is included. Other eqs. are the same as in Step 4. Note that in cases where initial temperature increase is very rapid, sub-steps are required in which the reaction enthalpy is gradually increased from 0 to 157 kJ/mol.

6) Pressure drop is calculated. This is the full set of model equations.

NOMENCLATURE

a : CO disappearance adsorption constant [1/MPa]
A, B, C, D, E : parameters in Eq. (40) [dimesionless]
a_{gl}, b_{gl} : coefficients of Matsuura et al. correlation [dimensionless]
a_M : Ma et al. model constant for CO [dimensionless]
A_{cs} : tube cross-section area [m^2]
b : parameter in Eq. (S.37)

b_M : Ma et al. model constant for H_2 (dimensionless)
c : constant describing chain length dependent 1-olefin desorption dependency with carbon number [dimensionless]
C_{CO}^S : molar liquid phase concentration of CO at the surface of the catalyst particle [mol/m^3]
C_p : heat capacity [J/(kg*K)]
$C_{p,G}$: gas phase heat capacity [J/(kg*K)]
$C_{p,L}$: liquid phase heat capacity [J/(kg*K)]
ΔC_p : overall change in heat capacity per mole of CO [J/(kg*K)]
C_{wax} : molar concentration of wax [mol/m^3]
D_i^{er} : effective radial diffusivity of species i [m^2/s]
$D_{e,CO}$: effective intraparticle diffusivity of CO in wax [m^2/s]
$D_{wax,CO}$: diffusivity coefficient of CO in FTS wax [m^2/s]
d_t : tube diameter [m]
d_p : particle diameter [m]
F_g : molar flowrate of gas phase [mol/s]
F_i : molar flowrate of component i [mol/s]
F_l : molar flowrate of liquid phase [mol/s]
F_{tot} : total molar flowrate [mol/s]
H_{CO} : Henry's law constant for CO [Pa*m^3/mol]
$H_{CO,0}$: parameter in Eq. (S.39) [bar]
ΔH_{CO} : parameter in Eq. (S.39) [bar]
H_f^θ : standard enthalpy of formation [J/mol]
ΔH_r : reaction enthalpy per mole of CO consumed [J/mol]
ΔH_r^θ : standard reaction enthalpy per mole of CO consumed [J/mol]
k : CO disappearance rate constant [mol/(g_{cat}*h*MPa^2)]
k_M : Ma et al. model rate constant [mol/(g_{cat}*h*MPa$^{0.28}$)]
k_j : detailed kinetics rate constant (unit dependent on the form of rate law)
K_j : detailed kinetics equilibrium constant (unit dependent on the form of rate law)
K_i : vapor-liquid equilibrium constant [dimensionless]
M_{CO} : CO molar mas [g/mol]
$M_{g,ave}$: average molecular weight of gas phase [kg/mol]
M_{wax} : wax molar mas [g/mol]
m_M : Ma et al. model denominator constant [dimensionless]
P : pressure [MPa]
P_{CO} : partial pressure of CO [MPa]
P_{H_2} : partial pressure of CO [MPa]
P_{H_2O} : partial pressure of CO [MPa]
P_{CO}^s : partial pressure of CO at the catalyst particle surface [Pa]
P_i^{vap} : vapor pressure of component i [MPa]
Pe : Pecklet number [dimensionless]
Pr : Prandtl number [dimensionless]
$(-R_{CO})$: rate of CO consumption [mol/(g_{cat}*h)]
$(-R_{H_2})$: rate of H_2 consumption [mol/(g_{cat}*h)]
$(-R_{H_2O})$: rate of H_2O formation [mol/(g_{cat}*h)]
R_j : rate of component j formation [mol/(g_{cat}*h)]
$R_{CH_4}^{Ma}$: rate of methane formation according to Ma et al. model [mol/(g_{cat}*h)]
$R_{CH_4}^{det}$: rate of methane formation according to detailed kinetics [mol/(g_{cat}*h)]
$R_{C_nH_{2n}}^{det}$: rate of 1-olefin formation according to detailed kinetics (n= 2, 3, …) [mol/(g_{cat}*h)]
$R_{C_nH_{2n+2}}^{det}$: rate of n-paraffin formation according to detailed kinetics (n=2, 3, …) [mol/(g_{cat}*h)]
$(-R_{CO})^{prod}$: rate of CO consumption obtained for product formation stoichiometry [mol/(g_{cat}*h)]
$(-R_{H_2})^{prod}$: rate of H_2 consumption obtained for product formation stoichiometry [mol/(g_{cat}*h)]
Re : Reynolds number [dimensionless]
[S] : coverage of vacant active sites [dimensionless]
S_j : selectivity of component j [dimensionless]
T : temperature [K]
UR : usage ratio [dimensionless]
u_s : superficial fluid velocity [m/s]
V_0 : wax close-packed hard sphere volume [cm^3/mol]
V_b : wax molar volume [cm^3/mol]
x_i : molar fraction of component i in liquid phase [dimensionless]
X_{CO} : CO conversion level [%]
x_G : molar fraction of gas phase [dimensionless]
y_i : molar fraction of component i in gas phase [dimensionless]
z_i : molar fraction of component i [dimensionless]

Greek Letters

α_n : growth probability for chain with n C-atoms [dimensionless]
ε_b : bed porosity [dimensionless]
e_p : particle porosity [dimensionless]
λ_g : gas phase thermal conductivity [W/(m*K)]
λ_l : liquid phase thermal conductivity [W/(m*K)]
μ_G : gas phase viscosity [Pa*s]
μ_L : liquid phase viscosity [Pa*s]
ρ_b : bed density [kg/m^3]
ρ_G : gas phase density [kg/m^3]
ρ_L : liquid phase density [kg/m^3]
ρ_p : particle density [kg/m^3]
ϕ_p : particle sphericity [dimensionless]
σ_{CO} : molecular diameter of CO [Å]
σ_{wax} : molecular diameter of wax [Å]
τ_p : particle tortuosity [dimensionless]

REFERENCES

1. I. C. Yates and C. N. Satterfield, *Energy Fuels*, **5**, 168 (1991).
2. M. Mandić, B. Todić, L. Živanić, N. Nikačević and D. B. Bukur, *Ind. Eng. Chem. Res.*, **56**, 2733 (2017).
3. W. Ma, G. Jacobs, T. K. Das, C. M. Masuku, J. Kang, V. R. R. Pendyala, B. H. Davis, J. L. S. Klettlinger and C. H. Yen, *Ind. Eng. Chem. Res.*, **53**, 2157 (2014).
4. B. Todic, W. Ma, G. Jacobs, B. H. Davis and D. B. Bukur, *Catal. Today*, **228**, 32 (2014).
5. B. Poling, J. Prausnitz and J. O. Connell, The Properties of Gases and Liquids, McGraw-Hill Education (2000).
6. H. Delmas and G. Froment, *Chem. Eng. Sci.*, **43**, 2281 (1988).
7. J. Delgado, *Heat Mass Transfer.*, **42**, 279 (2006).
8. D. Gunn, *Chem. Eng. Sci.*, **42**, 363 (1987).
9. C. Erkey, J. B. Rodden and A. Akgerman, *Can. J. Chem. Eng.*, **68**, 661 (1990).
10. L. Caldwell and D. S. Van Vuuren, *Chem. Eng. Sci.*, **41**, 89 (1986).
11. C. L. Yaws, P. K. Narasimhan and C. Gabbula, Yaws' Handbook of

Antoine Coefficients for Vapor Pressure (2nd Electronic Edition), Knovel.
12. J. M. Smith, H. Van Ness and M. Abbott, Introduction to Chemical Engineering Thermodynamics, McGraw-Hill Education (2005).
13. J. J. Marano and G. D. Holder, *Fluid Phase Equilib.*, **138**, 1 (1997).
14. G. M. Builder, https://www.psenterprise.com/products/gproms/modelbuilder.
15. F. Benyahia and K. E. O'Neill, *Part. Sci. Technol.*, **23**, 169 (2005).
16. A. Matsuura, Y. Hitaka, T. Akehata and T. Shirai, *Heat Transfer - Jpn. Res.*, **8**, 44 (1979).